RSC Advances

REVIEW

View Article Online
View Journal | View Issue

Cite this: *RSC Adv.*, 2019, **9**, 9907

Recent developments in the fabrication, characterization and implementation of MgH_2-based solid-hydrogen materials in the Kuwait Institute for Scientific Research

Mohamed Sherif El-Eskandarany

Hydrogen energy holds tremendous promise as a new clean energy option. It is a convenient, safe, versatile fuel source that can be easily converted to the desired form of energy without releasing harmful emissions. Hydrogen storage, which spans both hydrogen production and hydrogen applications, plays a critical role in initiating a hydrogen economy. Apart from the traditional methods used for hydrogen storage, Mg metal has been considered to be the most suitable candidate for application as a safe hydrogen storage material. However, Mg still has several technical problems that must be solved before such an attractive light metal can be considered for use in real applications. This review article aims to present and discuss the most recent research activities (2010–2018) that have been undertaken at the Kuwait Institute for Scientific Research (KISR) to develop and implement new categories of MgH_2-based nanocomposites. Comparisons between different catalytic agents used to enhance MgH_2 properties are presented and discussed in terms of structure, morphology, thermal stability, and kinetics.

Received 12th January 2019
Accepted 13th March 2019

DOI: 10.1039/c9ra00287a

rsc.li/rsc-advances

1. Background

Owing to the rapid growth of the human population and the escalating development of the heavy industrial sectors, a drastic increase in the mass production of fossil fuels (coal, oil and natural gas) is required. Based on this extreme expansion in energy demands, the worldwide production of oil and coal jumped from 2500 and 3000 Mt in 1971 to 4321 and 7269 Mt in 2017, respectively.[1] During the 1990's, the worldwide fuel consumption of oil exhibited a dramatic increase when many of the developed countries initiated their heavy industrial programs. However, fossil fuel reserves, in particularly oil, were sharply decreased and they remain the dominant source of energy and provide more than 80% of the worldwide energy supply.[1]

According to the environmental and health point of view, fossil fuels emit carbon dioxide and other harmful air pollutants such as SO_2 and NO_x when burned.[2,3] The uncontrolled growth of fossil fuel consumption and their corresponding harmful gases and released emissions has led to a wide variety of public health and environmental costs at the global level.[4,5] Fig. 1 summarizes the worldwide CO_2 emission in the period between 1971 to 2015 in terms of the quantity (a) and the fuel sources (b).[1] Taking oil as an example, the amount of CO_2 released from burning oil increased almost linearly from 14 000 Mt in 1971 to 22 500 Mt in 2000 (Fig. 1). As the oil consumption increased dramatically in the period between 2000 to 2015, the related released CO_2 emissions jumped in 2015 to 32 294 Mt, as presented in Fig. 1.[1] Although primary energy sources, which are not infinitely available, may not be sufficient to provide the amount of energy demanded in worldwide in the near future their production and consumption are expected to rise with the rapid growth of the population worldwide.

Nanotechnology and Advanced Materials Program, Energy and Building Research Center, Kuwait Institute for Scientific Research, Safat 13109, Kuwait. E-mail: msherif@kisr.edu.kw

Prof. Dr M. Sherif El-Eskandarany became a Principal Research Scientist at KISR in 2007. Before this, he worked as a First-Under-Secretary at the Ministry of Higher Education and Scientific Research in Egypt, and as a Full Professor at the Institute for Materials Research, Tohoku University, Japan. He has published more than 284 peer-reviewed papers in highly-cited international scientific journals and more than 200 papers in the proceedings of international conferences. He is also the author of six scientific books. He has completed 12 projects as the project leader/principle investigator. More recently, he was awarded five US patents for hydrogen storage materials and surface protective nanocoatings.

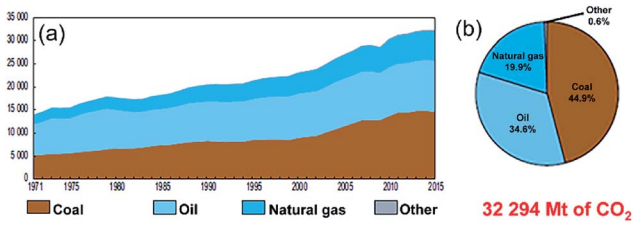

Fig. 1 (a) Worldwide CO_2 emissions (Mt of CO_2) from fuel combustion in the period between 1971 to 2015. The fuel shares of the CO_2 emissions from 2015 are shown in (b).[1]

2. Introduction

As discussed in the previous section, the energy sector is facing a big challenge to move towards a sustainable and clean energy future. Thus, maintaining the current linear consumption of fossil fuels is unrealistic. The depletion of fossil fuels is the key driver to finding alternative solutions to fuel our energy systems.[6] Versatile carbon-free energy carriers with a high-energy-density, such as hydrogen, are considered to be an alternative to fossil fuels. Accordingly, employing renewable and sustainable energy sources such as solar, wind and geothermal energies for developing clean and efficient energy systems has become one of the hottest research topics in the world and is attracting many scientists and researchers.

2.1 Hydrogen energy

Since the last decade, hydrogen has been widely proposed as a promising future alternative to replace fossil fuels and deliver the clean energy required in almost all sectors.[7] The relevance of hydrogen as an energy carrier is attributed to its unique properties of being convenient, safe, versatile,[8,9] easy to produce from renewable energy systems, and its ability to be converted to a desirable form of energy.[10,11] In addition, hydrogen has become a favorite energy carrier as it has a very high calorimetric value, with a lower heating value of 120 MJ kg^{-1} compared to petrol, which is approximately a third of this at 43 MJ kg^{-1}.[12]

However, hydrogen energy shows advanced properties and characteristics when compared with other sources of primary energy; the key advantage of hydrogen is that CO_2 is not produced when it is burned. Thus, hydrogen satisfies all concerns over air pollution and global warming, and the transition to use hydrogen as a fuel could be started well before the oil reserves are depleted.

2.2 Potential applications of hydrogen energy

Hydrogen fuel cells (FCs) have a wide range of potential applications, as they operate from a few watts up to gigawatts. Moreover, hydrogen has the potential to run a fuel-cell (FC) engine with greater efficiency than an internal combustion engine.[13,14] The same amount of hydrogen will take a FC-car at least twice as far as a car running on gasoline. Hydrogen micro-FCs have great potential for powering portable electronics such as laptops and mobile phones,[15] indeed, the superior energy density of a hydrogen polymer electrolyte membrane (PEM) micro-fuel cell could open up new pathways for manufacturing longer battery lifetimes.[16] For mobile applications, fuel cells could provide auxiliary power for electrical units such as air conditioning and refrigerators,[17] as well as electric cars[18] and vehicle powertrain applications.[19]

2.3 Hydrogen storage

The idea of hydrogen economy is based on the assumption that hydrogen gas can be produced by decomposing water using inexpensive primary sources of energy, such as solar energy, wind energy, tidal energy, or biomass decomposition.[20] Recent studies have highlighted the fact that hydrogen fuel costs are reasonable and can therefore be considered as an ideal candidate to replace fossil fuels as an energy carrier.[21] In fact, hydrogen storage is considered to be one of the most crucial factors for hydrogen economy, and one that governs the future utilization of hydrogen energy for real applications.[22]

2.3.1 Traditional techniques for hydrogen storage. Hydrogen can be stored in gaseous, liquid or solid states. The physical storing of hydrogen, which refers to pressurizing the gas under 350–700 bar into thick-wall cylinders made of high strength carbon fiber reinforced polymer (CFRP)[23] is the most common hydrogen storage approach. Obviously, using such pressurized hydrogen gas tanks as a source of fuel in vehicles is not safe and intensive research must be dedicated to improving the structural and mechanical properties of the materials used in the manufacture of the tanks.[24] Moreover, compressed hydrogen gas systems have low volumetric hydrogen storage densities.[25]

Cryo-compressed hydrogen storage (CcH_2) and liquid hydrogen (LH_2) storage are alternative mature approaches in which hydrogen is liquidized at −253 °C and compressed into vessels that can be pressurized to 250–350 atm. Accordingly, the size of the liquid hydrogen requires larger tanks, which are about three times larger than currently used gasoline tanks.[26] Moreover, liquid hydrogen requires well-insulated and expensive cryogenic storage vessels to prevent boil-off, maximize the dormancy and to maintain the temperature below 20 K.[27] Unfortunately, the gas–liquid transformation process is extremely expensive, consuming approximately about 25–30% of the energy content of the stored hydrogen.[28] Thus, employing these traditional storage approaches in real future applications may be difficult owing to the high cost and safety issues.[29]

At the beginning of this century, a new approach for hydrogen storage was developed by Aceves and his team.[30] This approach, the so-called cryogenic pressure vessel, attempted to combine the existing classic storage technologies (cryogenic and high pressure) to capture the advantages of both methods. The idea behind this cryo-compressed storage system was based on the design of a high-pressure (~350 bar) cryogenic pressure vessel and operation of the system at a low temperature (<20 K). Based on this, hydrogen could be stored at a significantly higher density than compressed hydrogen gas and probably an even higher density than liquid hydrogen.[30] This new technology has

received significant attention as the higher pressure can be attained in the vessel before the vent valve is activated. It is expected that this technology could reduce the boil off from liquid cryogenic hydrogen.[25]

2.3.2 Solid state hydrogen storage

Nanomaterials for hosting hydrogen. In contrast to the traditional methods used for hydrogen storage, nanomaterials, such as single-walled carbon nanotubes (SWCNTs)[31] and multi-walled carbon nanotubes (MWCNTs)[32] have received significant attention as a potential synthetic nano-media for solid-state hydrogen storage. It was reported that the storage capacity of hydrogen molecules that underwent physisorption at the SWCNTs bundles reached 8 wt% under 77 K.[33] The superior properties of SWCNTs, exemplified by their chemical stability, large surface area, hollowness, and light mass, were attributed to be responsible for the high storage capacity.[32]

Metal–organic framework (MOF) systems have shown beneficial properties for storing hydrogen by either physisorption or chemisorption processes.[34] However, these materials, with their extremely large specific surface areas and ultra-porous properties, can reach very high gravimetric hydrogen storage capacities; they typically possess a very low density and, therefore, a poor volumetric hydrogen storage capacity.[34] Likewise, MOF materials and complex hydrides such as amides, alanates and borohydrides do not often offer reversible hydrogen release, or require high temperatures.

Metal hydrides. The possibility of the formation of a metal hydride through the chemisorption concept was first reported in 1868 by T. Graham, when he discovered that metallic palladium (Pd) wires were readily charged by hydrogen.[35] Since then, it has been demonstrated by many researchers that hydrogen can be chemically stored in a wide spectrum of metals, metal alloys and intermetallic compounds in their solid state through the absorption process. More than 50 metallic elements of the periodic table can absorb hydrogen in different quantities and the possible choice of hydrogen storage materials are, therefore, enormous.[14]

Some solid-state metal hydrides possess excellent hydrogenation properties; such as high volumetric capacities, the capability to absorb hydrogen at a low pressure and temperature, reversibility, and hydrogen releasing through endothermic processes at moderate temperatures.[37] Moreover, certain metal hydrides have a higher hydrogen storage density (6.5 H atoms per cm^3 for MgH_2) than hydrogen gas (0.99 H atoms per cm^3) or liquid hydrogen (4.2 H atoms per cm^3).[36] Hence, metal hydride storage is a safe, volume-efficient storage approach that can be employed for onboard vehicle applications. Many scientific and engineering studies have been carried out in order to develop the absorption/desorption of hydrogen in metals for fuel cell applications.[38] In general, metal, intermetallic compounds and alloys can be separated based on their hydrogenation/dehydrogenation temperatures into two major groups as follows:

- Low-temperature metal hydrides, which release hydrogen under normal atmospheric pressure around room temperature, but have a hydrogen capacity that is restricted to be less than 2.15 wt% H_2 (*e.g.*, $FeTiH_{1.8}$ and $LaNi_5H_6$), and;
- High-temperature metal hydrides that possess a high hydrogen storage capacity by weight, but require high temperatures for hydrogen absorption/desorption. For example, commercial Mg can reversibly store about 7.6 wt%. The problems are the high operating temperature (300 °C) and the slow hydrogenation/dehydrogenation kinetics.

3. Magnesium hydride

Metallic Mg and Mg-based materials have been considering as the most important candidate hydrogen storage materials for use in real applications.[19–24,36] The worldwide interest in Mg is attributed to its natural abundance, low cost, light weight, and its high gravimetric (7.60 wt%) and volumetric (110 g l^{-1}) hydrogen storage capacities. Recently, it has been reported that waste Mg-based alloys such as Mg–Al[39] and Mg–Gd[40] were successfully used as feedstock materials to produce a good quality of MgH_2. More recently, the formation of Mg_2FeH_6 powders, starting from MgH_2 and plain carbon steel powders, that were used as precursors has been demonstrated by Polanski *et al.*[41] They claimed that magnesium iron hydride can be industrially manufactured at high yields using steel scrap, which can reduce the cost of the manufacturing process.

3.1 Traditional approaches for synthesizing bulk MgH_2

Theoretically, MgH_2 can be prepared by a direct reaction between Mg metal and hydrogen gas at normal pressure (~1 bar) and low temperature (~50 °C).[42] Unfortunately, in practice, this reaction cannot be achieved in such modest conditions owing to the poor hydrogenation kinetics.[43] In order to achieve a successful forward reaction with fast uptake kinetics, both the pressure and temperature must be increased to 70 bar and 350 °C, respectively.[43] These conditions are essential in order to supply the system with the pressure drive and thermal energy required to enhance the hydrogenation kinetics. Moreover, the heat treatment of Mg is very important to break down the oxide layer of MgO coating the Mg and hence allowing hydrogen atoms to diffuse into the fresh/clean surface of Mg.

In the classic methods used for preparing bulk MgH_2, the absorption process is achieved through two consecutive stages of physisorption followed by dissociation of the hydrogen molecules that are diffused throughout the hydride layer and nucleation of the hydride. In contrast to this, the dehydrogenation process starts with nucleation of the Mg metallic phase, and then the diffusion of hydrogen atoms throughout the Mg and hydride phase. Thus, the liberated hydrogen atoms are recombined at the Mg surface to form hydrogen molecules.[42] The rate-limiting process for desorption is the diffusion of the hydrogen through the hydride material.[43]

3.2 Synthesizing nanocrystalline MgH_2 powders by reactive ball milling

In spite of the traditional approaches used for the gas–solid reaction at relatively high temperatures, Calka *et al.*[44] and El-Eskandarany *et al.*[45] proposed a solid state approach called reactive ball milling (RBM), used for the preparation of different

families of metal nitrides and hydrides at ambient temperature. This mechanically-induced gas–solid reaction can be successfully achieved using either high- or low-energy ball milling methods. In both approaches, the starting metallic powders milled under a selected reactive gas atmosphere to produce dramatic lattice imperfections such as twinning and dislocations. These defects are caused by plastic deformation coupled with shear and impact forces that are generated by the ball-milling media.[46] The powders are, therefore, disintegrated into smaller particles with a large surface area, in which very clean or fresh oxygen-free active surfaces of the powders are created. Moreover, these defects, which are intensively located at the grain boundaries lead to separation of the micro-scale Mg grains into finer grains capable of the absorption of hydrogen atoms at the first atomically clean surfaces to form MgH_2 powders.[14]

3.2.1 High-energy reactive ball milling. Planetary ball mills are the most popular type of mills used in scientific research for synthesizing MgH_2 nanopowders. In this type of mill, the ball milling media (Fig. 2) has a considerably high energy, as the milling stock and balls are thrown off the inner wall of the vial (Fig. 3c) and the effective centrifugal force reaches up to 20 times gravitational acceleration.[14] The centrifugal forces caused by the rotation of the supporting disc and the autonomous turning of the vial act on the milling charge (balls and powders). As the turning direction of the supporting disc (Fig. 3c) and the vial are opposite to each other, the centrifugal forces are alternately synchronized and opposite. Therefore, the milling media and the charged powders alternatively roll on the inner wall of the vial, and are lifted and thrown off across the bowl at high speed, as schematically presented in Fig. 2.

In a typical experimental procedure, a certain amount of Mg (usually in the range between 3 to 10 g based on the volume of the vial) is balanced inside an inert gas atmosphere (argon or helium) in a glove box and sealed together with a certain number of balls (*e.g.*, 20–50 hardened steel balls) into a hardened steel vial (Fig. 3a and b), using, for example, a gas-temperature-monitoring system (GST). With the GST system, it becomes possible to monitor the progress of the gas–solid reaction taking place during the RBM process, as shown in Fig. 3c and d. The temperature and pressure changes in the system during the milling process can be also used to realize the completion of the reaction and the expected end-product

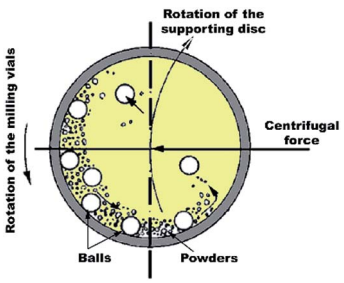

Fig. 2 Schematic diagram showing the ball-powder-ball collisions in a planetary high-energy ball mill.

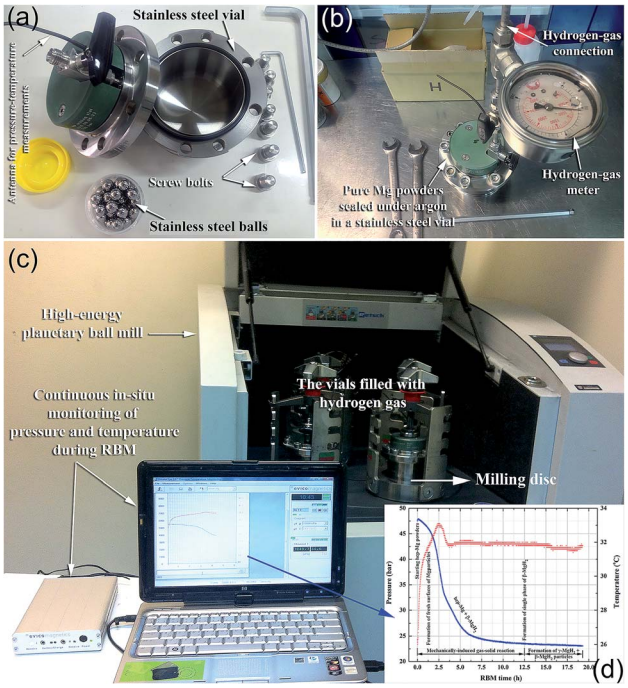

Fig. 3 Photographs taken from KISR-EBRC/NAM Lab, Kuwait, showing: (a) the vial and milling media (balls); and (b) the set up performed to charge the vial with 50 bar of hydrogen gas. The photograph in (c) presents the complete set up of the GST (supplied by Evico-magnetic, Germany) system prior to the start of the RBM experiment for preparing MgH_2 powders, using a Planetary Ball Mill P400 (provided by Retsch, Germany). The GST system allow us to monitor the progress of the RBM process, as demonstrated by temperature and pressure *versus* the milling time (d).

during the different stages of milling (Fig. 3d). The ball-to-powder weight ratio is usually selected to be in the range of between 10 : 1 and 50 : 1. The vial is then evacuated to the level of 10–3 bar before introducing H_2 gas to fill the vial with a pressure of 5–50 bar (Fig. 3b). The milling process is started by mounting the vial on a high-energy ball mill operated at ambient temperature.

3.2.2 Low-energy reactive ball milling. A tumbling mill is a cylindrical shell (Fig. 4a–c) that rotates about a horizontal axis (Fig. 4d).

Hydrogen gas is pressurized into the vial (Fig. 4c) together with the Mg powders and ball milling media, using a ball-to-powder weight ratio in the range between 30 : 1 to 100 : 1. The Mg powder particles meet the abrasive and impacting force (Fig. 4e), which reduce the particle size and create fresh-powder surfaces (Fig. 4f) ready to react with the hydrogen milling atmosphere. The useful kinetic energy generated in the tumbling mill can be applied to the Mg powder particles (Fig. 4e) by the following means: (i) collision between the balls and the powders; (ii) pressure loading of powders pinned between milling media or between the milling media and the liner; (iii) impact of the falling milling media; (iv) shear and abrasion caused by the dragging of particles between moving milling media; and (v) shock-wave transmitted through crop load by falling milling media.

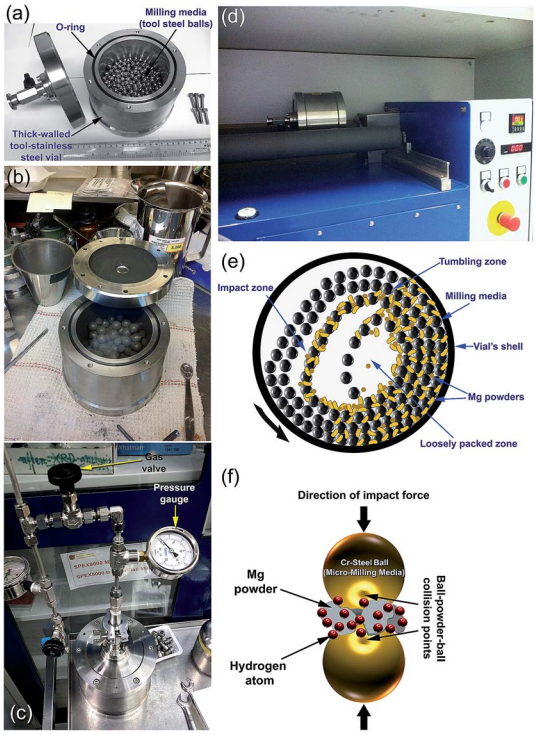

Fig. 4 Photos taken from the KISR-EBRC/NAM Lab, Kuwait display the set-up of a lab-scale roller mill (1000 M in volume) showing: (a) the milling tools including the balls (milling media and vial); (b) charging of Mg powders in the vial inside an inert gas atmosphere glove box; (c) evacuation set-up and pressurization of hydrogen gas in the vial; and (d) ball milling process using a roller mill. The schematic presentations show the ball positions and movement inside the vial of the tumbler ball mill in the dynamic mode (e), and a typical ball-powder-ball collision for a low energy tumbling ball mill is presented in (f).

One advantage of this type of mill is that a large amount of powder (100 to 500 g or more based on the mill capacity)[17] can be fabricated during each milling run. Thus, it is suitable for pilot and/or industrial scale MgH_2 production. In addition, the low-energy ball mill produces homogeneous and uniform powders when compared with the high-energy ball mill. Furthermore, such tumbling mills are cheaper than high-energy mills and are simply operated with low maintenance requirements. However, this kind of low-energy mill requires a long milling time (more than 300 h) to complete the gas–solid reaction and to obtain nanocrystalline MgH_2 powders.

3.3 Disadvantages of MgH_2

Unfortunately, and in spite of the attractive properties of MgH_2 there are certain major drawback issues restricting the implementation of this attractive solid-state hydrogen storage material in real applications.[46–49] MgH_2 in its pure form is very stable, possessing a large negative heat of formation (ΔH_{for} = −75 kJ mol^{-1} H_2)[50] and it shows slow kinetics of dehydrogenation at temperatures less than 400 °C.[51] In addition, Mg metal is very sensitive to the surrounding atmosphere, particularly to oxygen. Coating the powder with MgO and $Mg(OH)_2$ films during materials handling usually hinders the hydrogen atoms from penetrating the hard ceramic coating to react with Mg surfaces. Removal of these films requires a strict activation process of Mg under the application of a high hydrogen pressure (above 35 bar) and high temperature (~350 °C).[17] Furthermore, the low thermal conductivity of the MgH_2 system (0.4 W mK^{-1} (ref. 52)) is considered to be a serious problem as heat transfer is a very important factor that is required for both the hydrogenation and dehydrogenation processes.

4. Worldwide scenarios for improving the behavior of MgH_2

4.1 Alloying elements

One practical solution proposed for enhancing the hydrogenation/dehydrogenation properties of MgH_2 is to melt pure bulk Mg with selected alloying elements such as Ni, Pd, and Nd to obtain less stable binary, ternary or multicomponent Mg-based alloy systems with a lower heat of formation (ΔH_{for}). In many cases, the synthesized Mg-based alloy systems do not show attractive storage properties when compared with pure MgH_2. For example, alloying Mg with Ni to form binary Mg_2Ni lowers the ΔH_{for} of the metal hydride phase (Mg_2NiH_6) to −64.5 kJ mol^{-1} instead of −74.5 kJ mol^{-1} for pure MgH_2. However, the system shows a dramatic degradation in the hydrogen storage capacity (3.5 wt%) with no significant decrease in the decomposition temperature.[53]

At the beginning of this century, Yamada *et al.*[54] proposed the Mg-rich (90 at%) systems of Mg–Pd, Mg–Nd and Mg–Pd–Nd to replace the traditional Mg_2Ni alloy. They reported that Mg-based systems containing Pd at 300 °C demonstrate pressure-composition-temperature (PCT) curves with three plateau-like regions and a hydrogen absorbency of 5 wt%. They pointed out that the hydrogenation/dehydrogenation of the Mg–Nd system was influenced by the catalytic effect of the formed $NdH_{2.5}$ and NdH_3 phases which assisted the hydriding and dehydriding of the Mg matrix. For the Mg–Pd system, they reported that the disproportional reaction of Mg_6Pd to form Mg_5Pd_2 and MgH_2 retarded the overall reaction kinetics. In spite of their efforts dedicated to developing a new Mg-based alloy system with advanced kinetic behavior, their proposed $Mg_{89}Pd_7Nd_4$ alloy required 50 min to absorb about 4 wt% H_2 at 300 °C. In addition, achieving a complete dehydrogenation process for this system required 150 min at the same operating temperature.[54]

4.2 Doping with catalysts

Since the mid of 1990's, enormous efforts have been devoted to improving the hydrogenation/dehydrogenation behaviors of MgH_2, using a wide variety of catalysts. In this section, we will present typical examples of several attempts that have recently been reported to improve the kinetics of MgH_2 for hydrogenation and subsequent dehydrogenation.

4.2.1 Doping with metal and metal alloys catalytic agents. Owing to their superior capability for hydrogen splitting (dissociation) and re-combination, transition metal (TM) groups have received significant attention, particularly in 1990's

and 2000's. However, the effect of pure metals, such as Ti, Zr, V, Nb, Fe, Co, Ni, Pd, Pt, on the kinetic reactions of MgH_2 have been intensively studied for the past 20 years, and are still receiving great attention. Liang *et al.*[55] reported results obtained from doping MgH_2 powders with 5 wt% of Ti, V, Mn, Fe and Ni. In their work, the as-received MgH_2 powders were individually milled using a high-energy ball mill under an argon atmosphere for 20 h. They pointed out that elemental Ti and V showed better catalytic effects for hydrogen absorption and desorption compared to Ni. Since then, many researchers have reported attractive results upon using a wide range of pure metals.

Zaluska *et al.* reported the earliest study on the doping of MgH_2 powders with 3-d elements, when they selected Pd, Ti, Fe, V, Zr, and Mn for catalyzing MgH_2 powders, either individually or as a catalytic mixture.[56] The catalyzed MgH_2 powders were prepared by high-energy ball milling composite powders in the time range of 15 min to 20 h. Based on their findings, elemental V and Zr, as well as a composite of Mn/Zr, were determined to be the most effective agents used to improve the kinetic behavior of MgH_2. Some typical MgH_2/TM composite systems with their corresponding characteristics are listed in Table 1.

Intermetallic compounds and alloys have received a significant amount of attention since 1979 when Karty *et al.* reported their beneficial effect on the hydrogenation and dehydrogenation of Mg upon doping MgH_2 with a Mg_2Cu eutectic alloy.[60] The enhancement achieved in the kinetic reaction of MgH_2 was attributed to the dominant role of Mg_2Cu, which consisted of minimizing the oxide inhibition by providing a clean unoxidized external surface at which the hydrogen gas could readily adsorb, dissociate, and diffuse into the interior where hydride formation occurs; essentially the reverse process to that occurring in dehydriding.[60] Since then Mg has been doped with alloys of different concentrations, including Mg_2Ni,[61,62] $Mg(La_2Mg_{17})$–$LaNi_5$,[63] Mg–FeTi,[64] Mg–$ZrFe_{1.4}Cr_{0.6}$,[65] $LaNi_5$,[66] ZrCrNi,[67] and Ti–V based bcc alloys.[68]

Dehouche *et al.* demonstrated a detailed and useful study on the doping effect of activated $Zr_{100-x}Ni_x$ alloy powders on the uptake/release kinetics of MgH_2 powders.[69] They pointed out that catalyzing MgH_2 with activated ZrNi alloys led to a remarkable increase in the kinetic behavior of MgH_2. Their results have shown that the best kinetic properties of MgH_2 were obtained upon doping with 10 wt% of eutectoid $Zr_{47}Ni_{53}$, however, mixing with different compositions (Zr_9Ni_{11} and Zr_7Ni_{10}) also led to a significant improvement, but not as great as that observed for the eutectoid composition.[69] They found that when MgH_2/0.2 mol% Zr_7Ni_{10} is ground with activated carbon, a further kinetic improvement was attained. Table 2 lists selected intermetallic compounds and alloys that have been efficiently used as catalytic agents to enhance the kinetic behavior of MgH_2. Further information on different intermetallic compound catalytic agents has been previously reported in several different comprehensive review articles.[20,25,27,48,49,57]

4.2.2 Doping with refractory materials. Refractory materials are a group of inorganic non-metallic materials that possess extraordinary high values of hardness and compressive strength. Metals oxides, metal-carbides, -nitrides, and -hydrides are some typical examples. These chemically stable hard materials can withstand high temperatures without changes occurring to their crystal structures and their chemical/physical properties. Accordingly, these properties make them desirable materials for many industrial applications, such as chemical reactors, surface protective coating, and cutting tools. Since the 1990's, hard refractory powders have been used as heterogeneous catalysts to enhance the hydrogenation/dehydrogenation kinetics of MgH_2. A brief review showing their roles in improving the behavior of MgH_2 is detailed in this section.

Metal oxides possess a strong catalytic effect, leading to improvement of the hydrogenation/dehydrogenation kinetics of MgH_2. One of the earliest works was reported by Oelerich *et al.*[73] who prepared different systems of nanocrystalline Sc_2O_3, TiO_2, V_2O_5, Cr_2O_3, Mn_2O_3, Fe_3O_4, CuO, Al_2O_3, and SiO_2 powders using high-energy ball milling. The nanocrystalline oxide powders (5 wt%) were obtained after 20 h of milling, and were individually mixed with MgH_2 powders and then high-energy ball milled for a further 100 h under an Ar atmosphere. The results showed that all of the nanocrystalline oxides used in their study had a remarkable effect in improving the absorption/desorption kinetics of MgH_2.[73] They reported that composite materials containing Fe_3O_4 showed the fastest absorption kinetics at

Table 1 Effect of pure metal additives on the hydrogenation and dehydrogenation characteristics of MgH_2 powders[a]

Catalyst used	Dose	Doping approach	Hydrogenation/dehydrogenation properties	Apparent activation energy (kJ mol^{-1})	Ref.
NPs-Fe	10 wt%	Ar-HEBM/4 h	Absorption: 10 bar/350 °C: 5.1 wt%/9.1 min	86	57
NPs-Co	10 wt%	Ar-HEBM/4 h	Absorption: 10 bar/350 °C: 4.3 wt%/7.7 min	75	58
NPs-Ni	10 wt%	Ar-HEBM/4 h	Absorption: 10 bar/350 °C: 5 wt%/6.1 min	72	58
NPs-Cu	10 wt%	Ar- HEBM/4 h	Absorption: 10 bar/350 °C: 4.6 wt%/15.3 min	76	58
Zr	1 at%	H_2-RBM/300 rpm/20 h + annealing at 100 °C/40 bar H_2/24 h	Absorption: 5.5 wt%/4000 s/300 °C. Absorption of nanocomposite: 3.5 wt% H_2/6000 s/100 °C. Dehydrogenation: 5.5 wt% H_2/2000 s/350 °C	40	59

[a] HEBM: high-energy ball milling; RBM: reactive ball milling; NA: not available.

Table 2 Doping effects of intermetallic compounds and alloys on the hydrogenation and dehydrogenation behavior of MgH_2 powders[a]

Catalyst used	Dose	Doping approach	Hydrogenation/dehydrogenation properties	Apparent activation energy (kJ mol^{-1})	Ref.
$LaNi_5$	5 wt%	H_2-HEBM/40 h	Absorption: 20 bar/285 °C: 5.1 wt%/2700 s. Desorption: 285 °C: 5.1 wt%/1800 s	NA	63
Mg_2Ni	5 mol%	Ar-HEBM/3 h	Absorption: 20 bar/220 °C: 5.5 wt%/30 min. Desorption: 220 °C: 5.5 wt%/60 min	NA	62
$Ti_{0.4}Cr_{0.15}Mn_{0.15}V_{0.3}$	20 wt%	Ar-HEBM/3 h	Absorption: 20 bar/350 °C: 6.5 wt%/300 min	71.2	68
ZrCrNi	10 wt%	Ar-HEBM	Absorption: 5 bar/300 °C: 5.8 wt%/30 min. Desorption: 0.1 bar/300 °C: 5.8 wt%/45 min	NA	67
TiAl	14 wt%	H_2-RBM/4 h	Absorption: 1 bar/100 °C: 4 wt%/30 min. Desorption: 0.1 bar/240 °C: 4 wt%/7 min	65	70
$Ti_{0.05}Cr_{0.20}V_{0.75}$	10 wt%	H_2-RBM/4 h	Absorption: 1 bar/25 °C: 3 wt%/75 min. Desorption: 0.01 bar/240 °C: 5.5 wt%/5 min	71.2	71
FeTi	5 wt%	Ar-HEBM/8 h	Absorption: 30 bar/300 °C: 5.8 wt%/800 s. Desorption: 1.58 bar/300 °C: 2.57 wt%/110 min	NA	72
FeTiMn	40 wt%	Ar-HEBM/40 h	Absorption: 40 bar/80 °C: 4 wt%/3600 s. Desorption: 3 bar/240 °C: 2.57 wt%/7200 min	NA	72

[a] HEBM: high-energy ball milling; RBM: reactive ball milling; NA: not available.

300 °C, followed by V_2O_5, Mn_2O_3, Cr_2O_3, and TiO_2. In 2007, Aguey-Zinsou *et al.* ball-milled MgH_2 with 17 wt% Nb_2O_5 for 200 h, using a high-energy ball mill.[74]

Based on their results, pure MgH_2 revealed fast hydrogen sorption kinetics (Table 3) after a long milling time (700–1000 h) with Nb_2O_5. They attributed this remarkable improvement to a so called "process control agent" in which Nb_2O_5 plays three roles, a lubricant, dispersing and cracking agent.[74] Properties related to the selected MgH_2/metal oxides composite systems are shown in Table 3.

5. Kuwait Institute for Scientific Research

Kuwait Institute for Scientific Research (KISR, http://www.kisr.edu.kw/en/) is an independent, national institute of scientific excellence, and was established in 1967. Since then, KISR's role and responsibilities have expanded greatly to include the advancement of the national industry and the undertaking of studies to address key challenges, such as the preservation of the environment, sustainable management of Kuwait's natural resources, responsible management of water and energy, and development of innovative methods of agriculture. Today, KISR is home to over 580 researchers and engineers and over 100 laboratories, housed at nine locations.

As an outcome of KISR's Transformation Project in 2010, the Energy and Building Research Center (EBRC, http://www.kisr.edu.kw/en/facilities/energy-building/?research=1), has emerged and is the center's focus is on research and technology themes within the energy and building sectors. In the energy research sector, EBRC intends to support and facilitate the process for the transition to advanced and diversified sustainable energy generation, energy storage technologies through collaborative research, development, and knowledge transfer.

The building research sector addresses issues related to construction materials and existing and new infrastructure.

The Nanotechnology and Advanced Materials (NAM) Program (http://www.kisr.edu.kw/en/program/22/) is one of the EBRC's five programs. The program was established in 2010 in order to improve the performance and cost effectiveness of materials and devices required by the industrial sector through innovative solutions based on nanotechnology. Since then, the program has taken responsibility for supporting the most important and crucial problems in Kuwait, these are energy, water, petroleum, and oil.

5.1 Research activities devoted to enhancing the hydrogen storage properties of Mg

Since the establishment of the NAM Program it has been focused on the fabrication, characterization and implementation of new solid-hydrogen storage nanocomposite MgH_2 families. Fig. 5 shows three independent routes used for preparing nanocrystalline MgH_2 nanopowders.

In the first and second routes, high- and low-energy RBM under hydrogen pressure (Fig. 3 and 4) are employed to obtain γ- and β-MgH_2 phases after milling for 6–200 h. In the third route, the starting Mg-rods are subjected to severe plastic deformation, using the cold rolling (CR) process (Fig. 5). The cold rolled products obtained after 150–300 passes are charged

Table 3 Doping effects of selected metal oxides on the hydrogenation and dehydrogenation behavior of MgH_2 powders

Catalyst used	Dose	Doping approach	Hydrogenation/dehydrogenation properties	Apparent activation energy (kJ mol^{-1})	Ref.
Nb_2O_5	17 wt%	Ar-HEBM/ZrO_2 milling tools/200 h	Absorption: 300 °C: 6 wt%/120 s. Desorption: 300 °C: 6 wt%/300 s 10 cycles	NA	73
	5 wt%	Ar-HEBM/24 h MgH_2 + 20 min Nb_2O_5	Absorption: 10 bar/300 °C: 5.2 wt%/78 s. Desorption: 0.1 kPa/300 °C: 6 wt%/300 s	NA	73
	10 wt%	Ar-HEBM	Absorption: 5 bar/300 °C: 5.8 wt%/ 30 min. Desorption: 0.1 bar/300 °C: 5.8 wt%/350 min	NA	75
	14 wt%	H_2-RBM/4 h	Absorption: 1 bar/100 °C: 4 wt%/30 min. Desorption: 0.1 bar/240 °C: 4 wt%/7 min	65	76
TiO_2	20 wt%	H_2-RBM/1 h/8 bar	Absorption: 20 bar/350 °C: 3.8 wt%/ 2 min. Desorption: 1 bar/350 °C: 4.4 wt%/ 8.5 min	NA	77
Fe_2O_3	10 wt%	H_2-RBM/10 bar	Absorption: 12 bar/320 °C: 4.22 wt%/ 10 min	NA	78
Cr_2O_3	1.2 wt%	Ar-HEBM	Absorption: 10 bar/300 °C: 6.4 wt%/ 5 min. Desorption: 0.25 bar/300 °C: 6.4 wt%/20 min	NA	79
Fe_3O_4@graphene	5 wt%		Absorption: 15 bar/290 °C: 6.2 wt%/ 2.5 min 25 cycles	90.53	80
La_2O_3	12 wt%	Ar-HEBM/20 h	Absorption: 10 bar/300 °C: 4.75 wt%/ 8 min. Desorption: 0.3 bar/300 °C: 6 wt%/ 25 min	NA	81

using high-energy RBM and milled for 100 h to obtain MgH_2 powders (Fig. 5). The obtained MgH_2 powders are subjected to further grain refining, using the cold rolling process for 50–100 passes. The end-product powders obtained through each preparation route are doped with 5–10 wt% of one catalytic agent and then milled under hydrogen for 50 h. The catalytic systems used here can be classified into five groups based on their nature (Fig. 5), namely: (i) metal oxide and metal carbides;

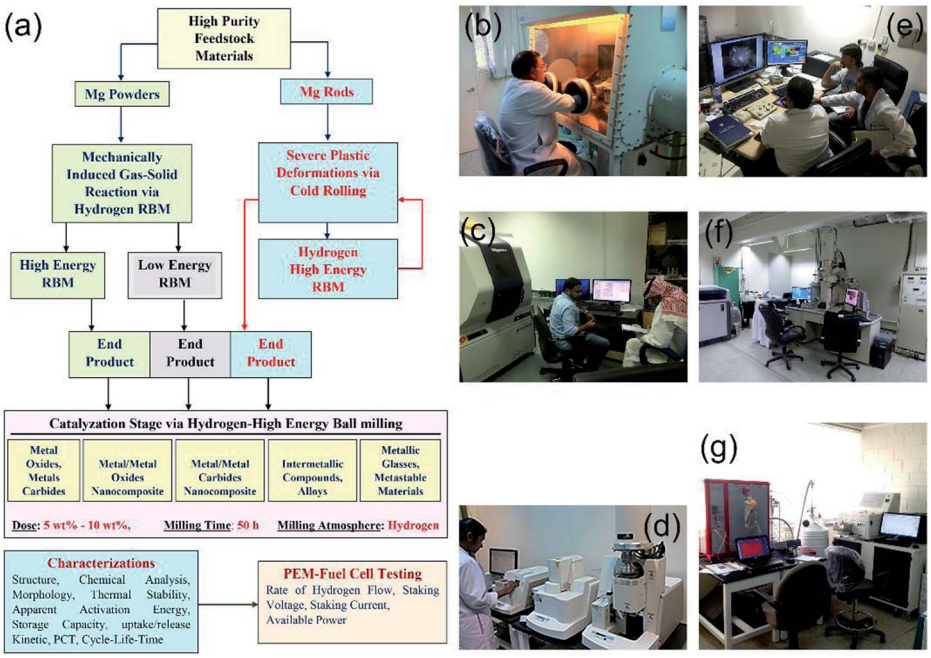

Fig. 5 (a) Flowchart diagram presenting two approaches employed in KISR for preparing nanocrystalline MgH_2 powders, using high- and low-energy RBM techniques under hydrogen gas pressure. The chart elucidates the two approaches (cold rolling and catalyzation) utilized to improve the hydrogen storage behavior of MgH_2. Some of the routine characterization techniques for MgH_2-based materials, including FC testing are presented in (a). The figure presents the ways of handling the materials inside an atmosphere control glove box (b), and onsite photos of some of the equipment used for characterization are presented in (c–g).

(ii) metal/metal oxide nanocomposite; (iii) metal/metal carbides nanocomposite; (iv) intermetallic compounds and alloys; and (v) metallic glasses and metastable materials.

5.1.1 Novel approach for doping MgH_2 with pure metals. In parallel to the worldwide efforts being paid to enhancing the behavior of MgH_2 by using a long list of metallic catalysts, researchers have recently developed a new cost effective method called the *in situ* catalyzation approach.[82] In this method, Ni-balls were used as milling media during the RBM of Mg under 50 bar of H_2.

After high-energy ball milling for 6 h, Ni shots (approximately 65 nm in size) worn out from the Ni-balls were embedded into the MgH_2 matrix, as shown in Fig. 6a. Increasing the RBM time (12.5–25 h) led to a monotonical decrease in the Ni particle size and an improvement in the Ni particles distribution in the MgH_2 matrix (Fig. 6d and g).

Towards the end of the processing time (50 h) nano-Ni powders (~5 nm) were homogeneously embedded into the matrix to form uniform nanocomposite powders with an Ni concentration of 5.5 wt% ± 0.21, as displayed in Fig. 6k and l. MgH_2/5.5 wt% Ni nanocomposite powders obtained after a short RBM time (25 h) revealed low values for the decomposition temperature (218 °C), at which the apparent activation energy (E_a) was 75 kJ mol^{-1}.[83] In addition, the hydrogenation (Fig. 7a)/dehydrogenation (Fig. 7b) kinetics measured for a sample at moderate temperature (275 °C) for 25 h were found to be 2.5 min and 8 min to uptake and release 5.8 wt% H_2, respectively. The authors claimed that this fast kinetic behavior was attributed to the formation of a homogeneous nanocomposite system, in which nano-powders were adhered to all MgH_2 powders without exception.[83] The synthesized nanocomposite was able to perform 100 continuous cycle-life times of hydrogen charging/discharging at 275 °C within 56 h without failure or degradation, as elucidated in Fig. 7c.

More recently, Ti balls have been used as milling tools for RBM of Mg under a hydrogen (50 bar) atmosphere.[46] Similarly to the Ni-balls, Ti shoots were worn out from the Ti-balls and embedded in the MgH_2 matrix to form uniform nanocomposite MgH_2/5.3 wt% Ti powders after 50 h (Fig. 8a). The measured decomposition temperature and calculated E_a of this nanocomposite system obtained after 50 h of milling were 230 °C and 72 kJ mol^{-1}, respectively.[46] The hydrogenation kinetics for the sample obtained after 50 h of RBM (end product) were investigated under 10 bar of H_2 at applied temperatures of 100, 125, 150 and 175 °C, as presented in Fig. 8b. The sample showed outstanding hydrogenation behavior at a very low temperature (100 °C), demonstrated by the short time required to absorb 4.9 wt% H_2 in 3 min (Fig. 8b). At 175 °C, a better storage capacity and kinetics were attained, as indicated by the short time required (3 min) to uptake 5.2 H_2, as shown in Fig. 8b.

The dehydrogenation kinetic behaviors for the sample obtained after 50 h of RBM time were investigated at different temperatures in a range between 175 °C and 250 °C (Fig. 8c). This sample possessed moderate dehydrogenation kinetics in a low temperature range (175 to 225 °C), indicated by the short time (4 min) necessary to release −2.1 and −3 wt% hydrogen, respectively, as displayed in Fig. 8c. Obviously, the kinetics of the sample were enhanced by increasing the dehydrogenation time to 7 min, the hydrogen release increased with the increasing applied temperature from −3.7 wt% (175 °C) to −4.9 wt% (200 and 225 °C), respectively. The two samples measured at 225 °C and 250 °C reached to saturation values of −5.1 and −5.5 wt% H_2, respectively after 10 min, as indicated in Fig. 8c.

5.1.2 Catalyzation with metal oxide nanopowders. Efforts have been made in part to enhance the behavior of MgH_2 by doping with Nb_2O_5 nanopowders. In the experiments, the as-prepared MgH_2 powders obtained after 200 h of RBM were doped, first with 2.5, 5, and 10 wt% of the Nb_2O_5 nanopowders, and were then subjected to HBM under hydrogen for 50 h.[84] The hydrogenation/dehydrogenation kinetics were examined for pure MgH_2, and the MgH_2/x wt% Nb_2O_5 (x; 2.5, 5, 10) powders in a temperature range between 200–250 °C, as displayed in Fig. 9.

The absorption kinetics investigated at 200, 225 and 250 °C for the pure MgH_2 nanocrystalline powders obtained after 200 h of RBM time (Fig. 9a) were faster when compared with the powders obtained after a short milling time.[84] After this long milling run, the powders were subjected to dramatic grain refining associated with severe lattice imperfections. This led to drastic powder disintegration and the formation of ultrafine grains ranging between 5 and 8 nm in diameter.[84]

These favorable morphological properties led to an enhancement in the uptake kinetics, even at a relatively low

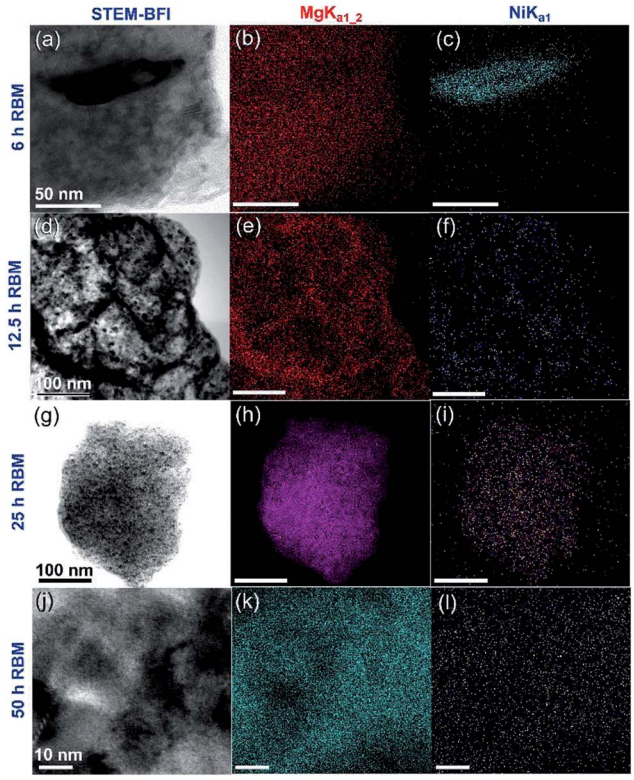

Fig. 6 (a, d, g and j) STEM-BFIs; (b, e, h and k) Mg-Kα_{1-2}; and (c, f, i and l) Ni-Lα_1 for the powders obtained after different stages of RBM, using a milling media of Ni-balls.[83]

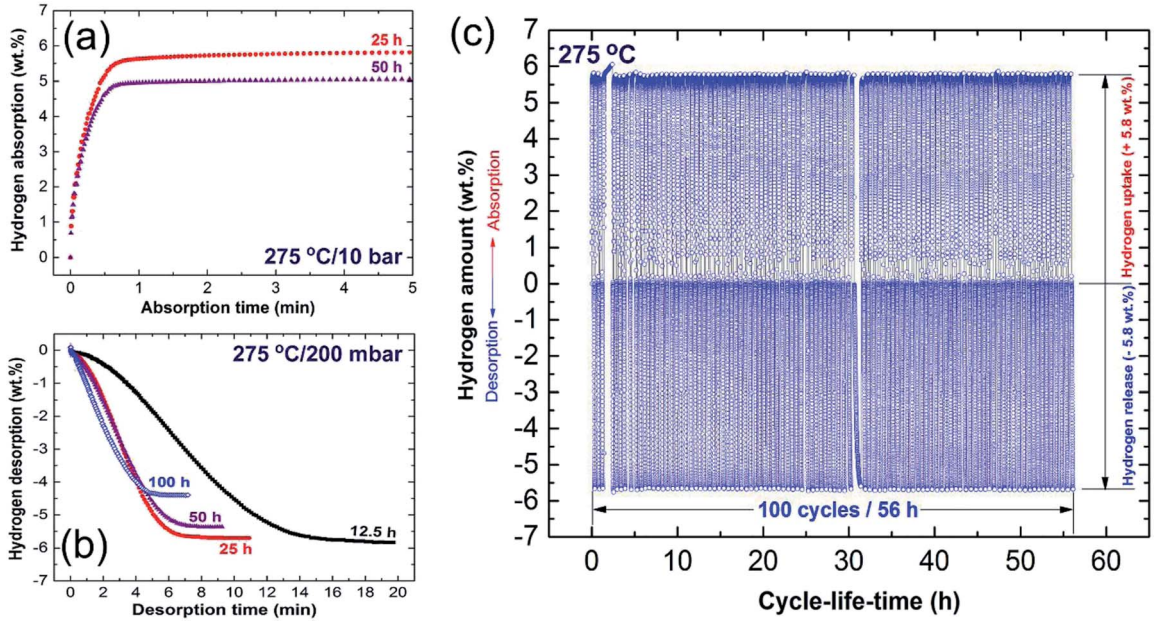

Fig. 7 (a) Hydrogenation; and (b) dehydrogenation kinetics examined at 275 °C for MgH_2 powders obtained after different RBM times, using a milling media of Ni-balls. The cycle-lifetime conducted at 275 °C for the sample obtained after 25 h of RBM time is presented in (c).[86]

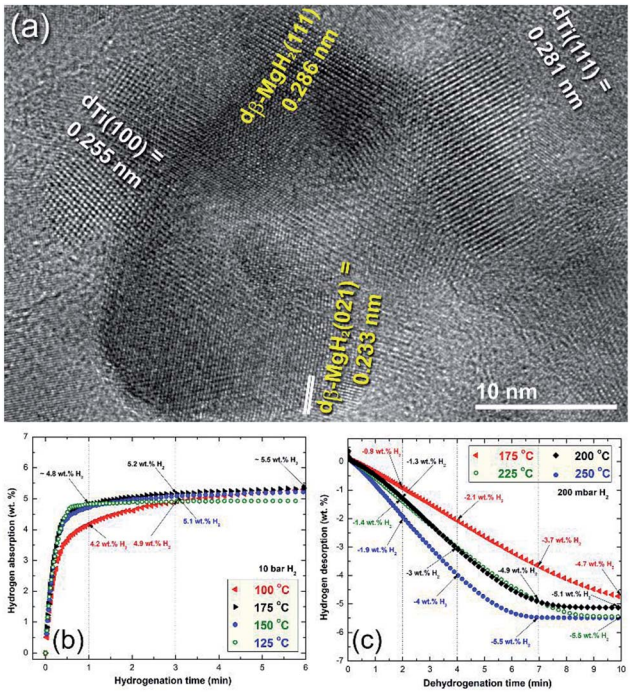

Fig. 8 (a) Field emission-high resolution transmission electron microscopy (FE-HRTEM) image of MgH_2 powder containing about 5 wt% Ti metallic particles after 50 h of RBM, using a milling media of Ti-balls. The hydrogenation and dehydrogenation kinetics measured at different temperatures for a 50 h sample are presented in (b) and (c), respectively.[46]

temperature of 200 °C. For example, at this temperature the sample absorbed about 3.5 wt% H_2 within 500 s and approached 6.3 wt% H_2 after about 2500 s, as shown in Fig. 9a. When these values are compared with those obtained at 225 °C (4.9 wt% H_2/500 s and 6.8 wt% H_2/2500 s) and 250 °C (5.49 wt% H_2/500 s and 6.81 wt% H_2/2500 s), it can be seen that a small increase in the applied temperature led to a significant improvement in the kinetics of hydrogen absorption for the nanocrystalline MgH_2 powders (Fig. 9a).

Nanocrystalline MgH_2 powders obtained after 200 h of RBM possessed slow desorption kinetics at 200 °C and 225 °C, however, they showed moderate kinetics at 250 °C, indicated by the release of 6.51 wt% H_2 after 7500 s, as presented in Fig. 9b.

Doping MgH_2 with very small amount of Nb_2O_5 powders and then milling for 50 h led to a significant improvement in the absorption kinetics, exemplified by the ability of the powder to uptake about 4.5, 5.3, and 5.8 wt% H_2 at 200, 225, and 250 °C, respectively (Fig. 9c). At 250 °C, nanocomposite MgH_2/2.5 wt% Nb_2O_5 reached a saturated value of 6.1 wt% H_2 after 600 s, as shown in Fig. 9c. The corresponding desorption kinetics showed an outstanding improvement, as suggested by the short time (800 s) required to desorb 6.1 wt% H_2 at 250 °C (Fig. 9d). Further comparison between the hydrogen storage properties of the starting synthetic MgH_2 and MgH_2/x wt% Nb_2O_5 (x; 2.5, 5, 10) are presented in Table 4. The improvement achieved in the kinetic behavior of the MgH_2 powders upon milling with Nb_2O_5 powders was attributed to the micro-cracking effect induced by the hard spherical Nb_2O_5 powders. Moreover, it is believed that it can act as effective catalyst in its recombination with hydrogen molecules and accelerate the promotion of the gas–solid reaction.[84]

5.1.3 Catalyzation with metal/metal oxide nanocomposite powders. This work aimed to study the synergetic effect of two different types of catalysts (Ni and Nb_2O_5) on enhancing the hydrogen storage properties of nanocrystalline MgH_2

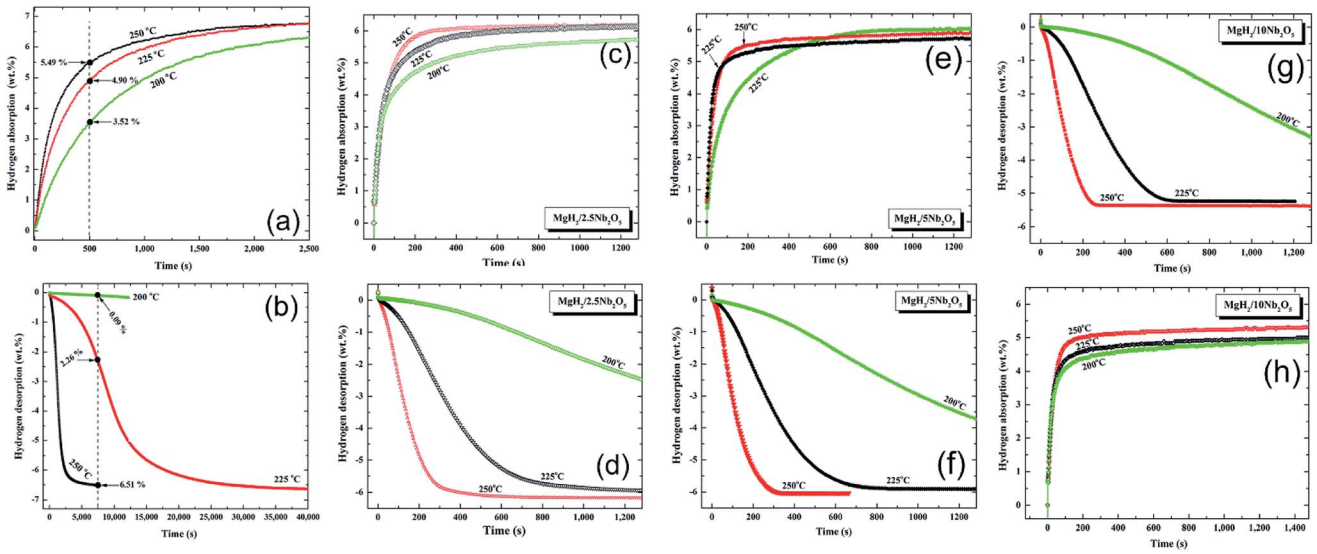

Fig. 9 Effect of Nb_2O_5 doping dose and applied temperature on the hydrogenation (a, c, e, g), and dehydrogenation (b, d, f, h) kinetics of the MgH_2 powders.[84]

powders.[87] The as prepared MgH_2 was doped with 5 wt% Ni and 5 wt% Nb_2O_5 and underwent high energy ball milling (HEBM) under H_2 for 50 h. The results showed that the hydrogenation/dehydrogenation kinetics of MgH_2 were enhanced by using the binary Ni/Nb_2O_5 system, as implied by the shorter time required for absorption when compared with the MgH_2/5 Nb_2O_5 system. This can be attributed to the elemental Ni additive, which is well known as a hydrogen splitting element. The cycle-life-time of the nanocomposite MgH_2/5Ni/5Nb_2O_5 powders is displayed in Fig. 10. This ternary nanocomposite system shows excellent storage properties, demonstrated by a high cyclic stability even after approximately 94 h (~180 cycles) with no obvious degradation in the hydrogen storage capacity, which exhibited almost constant absorption and desorption values of +5.44 and −5.46 wt% H_2, respectively, as displayed in Fig. 10.

5.1.4 Catalyzation with metal carbide nanopowders. Micro-milling media refers to abrasive hard material powders such as TiC that produce ultrafine hydride powders when ball milled with MgH_2 powders.[85] We succeeded to prepare ultrafine spherical $Ti_{55}C_{45}$ particles (~15 nm in diameter; Fig. 11a), using a mechanically induced self-propagating reaction.[86] The sphericity and fineness of the TiC allowed these hard powders to be embedded and occupy catalytic sites at the grain boundaries of the Mg matrix, as presented in Fig. 11b. The Metal carbide powder played a vital role in hindering Mg grains from growing during practical use at a moderate temperature of 275 °C.[87] Accordingly, the end-product of the nanocomposite MgH_2/5 wt% TiC obtained after 50 h of ball milling revealed an excellent absorption/desorption cyclability of 530 complete cycles with no degradation, as shown in Fig. 11c.[85] In addition, during the repeat absorption/desorption cycles hard spherical TiC powders penetrated into MgH_2 surfaces to form groves, as shown in Fig. 11d. Formation of such grooves facilitated excellent hydrogen diffusion paths.[87] The as fabricated nanocomposite MgH_2/5TiC powders possessed superior hydrogenation/dehydrogenation characteristics, indicated by the low value of the activation energy (97.74 kJ mol^{-1}), and the short time required to achieve complete absorption (6.6 min) and desorption (8.4 min) of 5.5 wt% H_2 at a moderate temperature of 275 °C under a hydrogen gas pressure ranging from 0 bar to 8 bar.[87]

5.1.5 Catalyzation with intermetallic compounds powders. Among the different intermetallic alloys prepared by arc melting, two binary alloy systems of $Mn_{3.6}Ti_{2.4}$ (ref. 88) and $ZrNi_5$ (ref. 89) alloys showed a good potential for use as catalysts. The end-product of the MgH_2/7 $Mn_{3.6}Ti_{2.4}$ nanocomposite powders obtained after 50 h of RBM were aggregated to form particles with an apparent particle size of about 250 nm in diameter (Fig. 12a). These aggregates consisted of MgH_2 (Fig. 12b) doped with nano-sized $Mn_{3.6}Ti_{2.4}$ dispersoids (Fig. 12c and d). At this final stage of ball milling, the $Mn_{3.6}Ti_{2.4}$ particles possessed a lens-like morphology with particle size distribution lying in the range between 8 and 32 nm in diameter, as displayed in Fig. 12c and d, respectively. Owing to the good distribution of the $Mn_{3.6}Ti_{2.4}$ nano-lenses in the MgH_2 matrix, the end product of this system revealed good hydrogenation/dehydrogenation kinetics at a moderate temperature of 275 °C.[88] This is implied by the short time required to absorb and desorb ~5.3 wt% H_2 within 2 (Fig. 13a and b) and 7 min (Fig. 13c and d), respectively.

The formation of ultrafine nano-scaled powder particles facilitated a good hydrogen diffusion cyclability, as suggested by the long (1400 h) absorption/desorption cycle-life-time presented in Fig. 13e. However, a minor degradation (~0.3–0.4 wt% H_2) in the hydrogen storage capacity was observed between 400 h (300 cycles) and 1400 h (1000 cycles), as elucidated in Fig. 13e. This minor degradation took place because the slight grain growth came off in the Mg/$Mn_{3.6}$ $Ti_{2.4}$ grains, as indicated in Fig. 13f and g.[88]

More recently, nanocomposite MgH_2/10 wt% $ZrNi_5$ powders were fabricated in KISR by RBM the synthesized nanocrystalline MgH_2 with 10 wt% of arc-melt $ZrNi_5$ powders for 50 h.[89] Fig. 14

Table 4 Hydrogen storage properties of nanocrystalline MgH_2-based Nb_2O_5 prepared by the NAM Program/EBRC/KISR[a]

Catalyst used/dose	Doping approach	Hydrogenation/dehydrogenation properties	Apparent activation energy (kJ mol^{-1})	Ref.
MgH_2				
	H_2-RBM/50 bar/200 h	Absorption 200 °C: 6.3 wt%/10 bar/2500 s 225 °C: 6.4 wt%/10 bar/2500 s 250 °C: 6.5 wt%/10 bar/2500 s Desorption 225 °C: 6.4 wt%/0.02 bar/40000 s 250 °C: 6.5 wt%/0.02 bar/7500 s	134	87
Nb_2O_5				
2.5 wt%	H_2-RBM/50 bar/50 h	Absorption 200 °C: 5.7 wt%/10 bar/1250 s 225 °C: 5.9 wt%/10 bar/1000 s 250 °C: 6.1 wt%/10 bar/600 s Desorption 200 °C: 2.5 wt%/0.02 bar/1250 s 225 °C: 5.8 wt%/0.02 bar/1250 s 250 °C: 6.1 wt%/0.02 bar/800 s	NA	84
5 wt%	H_2-RBM/50 bar/50 h	Absorption 200 °C: 6.0 wt%/10 bar/1250 s 225 °C: 6.0 wt%/10 bar/800 s 250 °C: 6.0 wt%/10 bar/600 s Desorption 200 °C: 3.7 wt%/0.02 bar/1250 s 225 °C: 6.0 wt%/0.02 bar/1000 s 250 °C: 6.0 wt%/0.02 bar/280 s	104	84
10 wt%	H_2-RBM/50 bar/50 h	Absorption 200 °C: 4.8 wt%/10 bar/1400 s 225 °C: 5.0 wt%/10 bar/1200 s 250 °C: 5.4 wt%/10 bar/500 s Desorption 200 °C: 3.3 wt%/0.02 bar/1250 s 225 °C: 5.3 wt%/0.02 bar/700 s 250 °C: 5.4 wt%/0.02 bar/280 s	NA	84
Ni/Nb_2O_5				
5 wt%/5 wt%	H_2-RBM/50 bar/50 h	Absorption 200 °C: 5.2 wt%/10 bar/250 s 225 °C: 5.2 wt%/10 bar/220 s 250 °C: 5.4 wt%/10 bar/190 s Desorption 200 °C: 5.4 wt%/0.02 bar/2000 s 225 °C: 5.5 wt%/0.02 bar/500 s 250 °C: 5.5 wt%/0.02 bar/190 s	74	84

[a] HEBM: high-energy ball milling; RBM: reactive ball milling; NA: not available.

displays the temperature and time effects on the hydrogen absorption (a and b) and the consequent desorption (c and d) kinetics of the nanocomposite MgH_2/10 wt% $ZrNi_5$ powders obtained after 50 h of ball milling time. The synthesized nanocomposite powders showed a good potential for absorbing hydrogen gas in a wide temperature range (50–275 °C) with a different hydrogen capacity, as shown in Fig. 14a. After 0.5 min, the powders absorbed 4.6 wt% H_2 at 250 °C and 275 °C (Fig. 14b). In contrast, at this absorption time, the samples examined at 150, 100, and 50 °C revealed a modest hydrogen gas uptake that reached 0.8, 0.1, and 0.0 wt% H_2, respectively (Fig. 14b).

Increasing the hydrogen gas uptake time to 1 min led to a magnificent improvement of the absorbed hydrogen gas concentration, reaching 5.1 and 5.3 wt% at an applied temperature of 250 and 275 °C, respectively as shown in Fig. 14b. The samples examined at 150 and 100 °C showed a significant improvement, suggested by a dramatic increase in the hydrogen gas absorbed, reaching 3.8 and 2.2 wt%, respectively (Fig. 14b).

A marginal improvement in the absorption kinetics was observed for the sample measured at 50 °C, which absorbed only 0.2 wt. H_2 after 1 min, as displayed in Fig. 14b. Increasing the absorption time to 30 min (Fig. 14a) did not lead to an

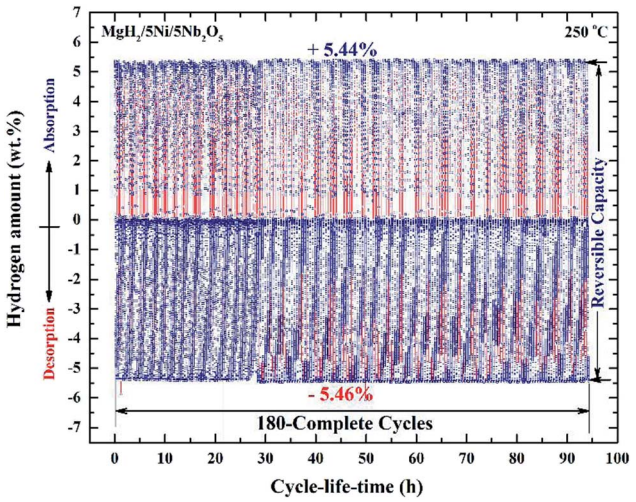

Fig. 10 Hydrogen absorption and consequent desorption curves of 180 complete cycles of nanocomposite MgH_2/5 wt% Ni/5 wt% Nb_2O_5 powders examined at 250 °C under a hydrogen pressure of 10 bar (absorption) and 200 mbar (desorption).[84]

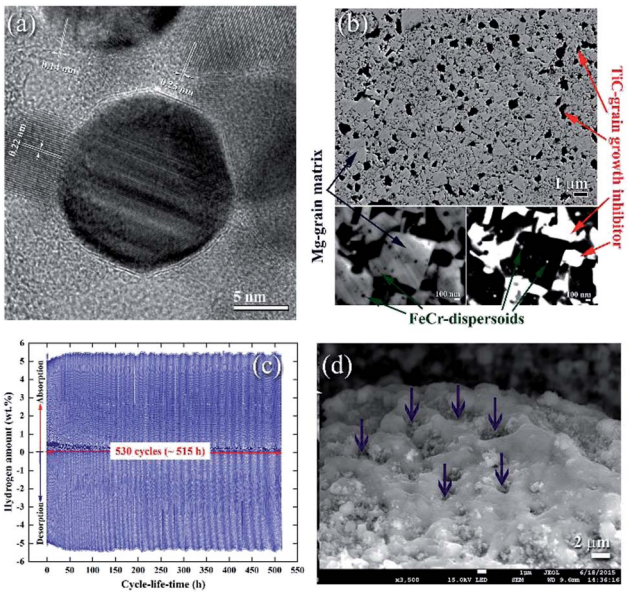

Fig. 11 (a) FE-HRTEM image of an as-prepared $Ti_{55}C_{45}$ particle, using the mechanically induced self-propagating reaction.[89] Low magnification FE-SEM, (b) high-magnification FE-SEM and (c) backscattered electron (BSE) micrographs of the cross-sectional view for the nanocomposite powders obtained after 50 h of ball milling and then hot-pressed in a vacuum at 525 °C under a uniaxial pressure of 125 MPa. The hydrogenation and consequent dehydrogenation curves conducted at 275 °C of 530 complete cycles performed within 515 h for nanocomposite MgH_2/5TiC powders obtained after 50 h of ball milling time are shown in (c). The FE-SEM micrograph of the powders obtained after the completion of 530 cycles is presented in (d).[90]

increase in the absorbed amount of hydrogen for the sample examined at 250 and 275 °C that tended to be saturated at 5.3 wt% H_2.

An outstanding improvement in the hydrogen concentration (4.4 wt%) absorbed at 150 °C could be attained after 30 min and

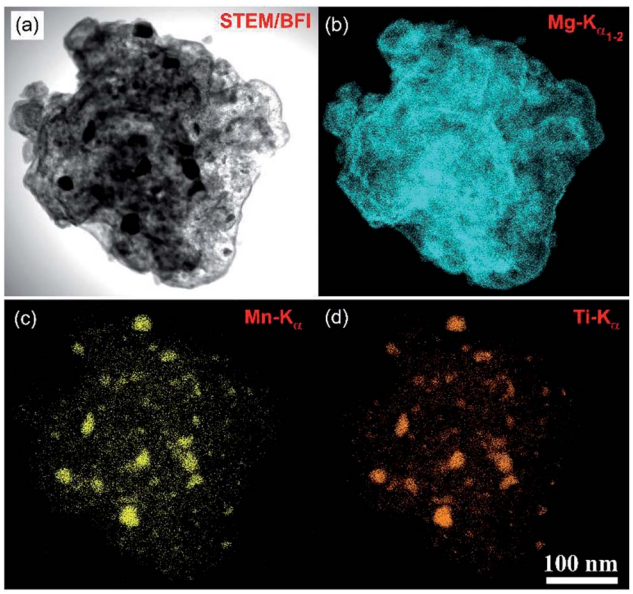

Fig. 12 (a) STEM-BFI and the corresponding X-ray elemental mapping of: (b) Mg; (c) Mn; and (d) Ti of nanocomposite MgH_2/7 wt% $Mn_{3.6}Ti_{2.4}$ powders obtained after 50 h of milling time.[88]

tended to increase to a higher value (4.9 wt%) after 103.8 min (Fig. 14a). After 30 min, the samples examined at 100 and 50 °C, absorbed approximately 3.4 and 0.9 wt% H_2, as shown in Fig. 14a. The hydrogen concentrations of these samples reached 4.2 and 2.5 wt% after 103.8 min (Fig. 14a). Approximately 180 min was required for the samples measured at 100 and 50 °C to absorb 4.4 and 3.1 wt% H_2, as elucidated in Fig. 14a.

The corresponding desorption kinetics for the nanocomposite powders investigated at 250 and 275 °C are shown in Fig. 14c and d. The sample examined at 275 °C showed excellent desorption kinetics, demonstrated by the relatively short time (~5 min) required to release approximately −4.4 wt% of hydrogen (Fig. 14d). This sample reached a very close saturation value (−5.2 wt% H_2) after only 10 min, as shown in Fig. 14d. The sample measure at 250 °C took about 5 and 10 min to release about −1.1 and −2.4 wt% H_2, respectively, as shown in Fig. 14d. After 15 min of desorption time (Fig. 14c), the samples examined at 275 and 250 °C released about −5.3 and −3.8 wt% H_2, respectively. About 40 min was required for the sample examined at 250 °C to desorb its full hydrogen storage capacity (−5.1 wt% H_2), as shown in Fig. 14c. This hydrogen storage nanocomposite system revealed a good cyclability (600 complete cycles), conducted at 275 °C without serious kinetic degradation.[89]

5.1.6 Catalyzation with metastable phases of Zr-based nanopowders. The idea of utilizing Zr-based metastable phases for improving the hydrogenation and dehydrogenation kinetics of MgH_2 systems dates back to 2015, when El-Eskandarany *et al.*[11] doped the hydride phase with 10 wt% of big-cube Zr_2Ni nanopowders. The results showed that high energy milling of MgH_2 with big-cube hard particles for 50 h led to superior storage properties of MgH_2 powders, as indicated by the short time required to absorb and desorb 5.1 wt% H_2 within

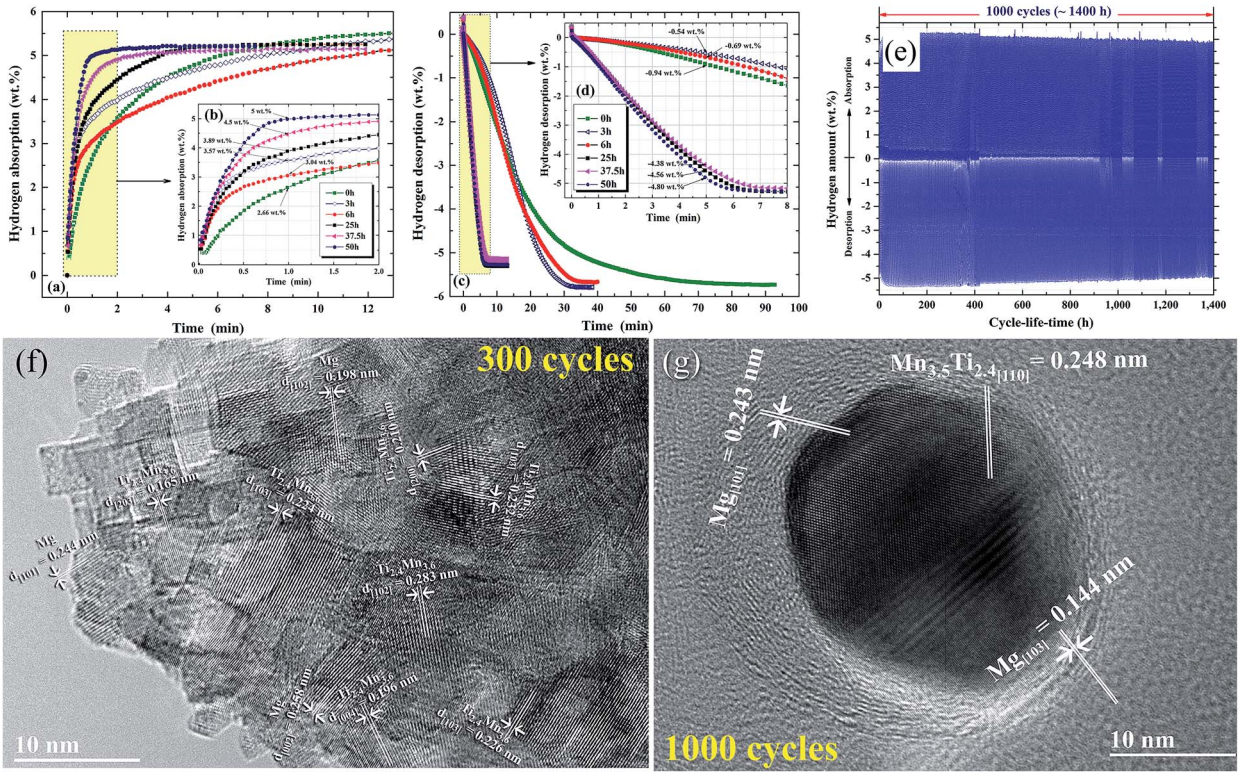

Fig. 13 Effects of ball milling time on the (a and b) hydrogenation and (c and d) dehydrogenation kinetics of nanocomposite MgH_2/7 wt% $Mn_{3.6}Ti_{2.4}$ powders. The hydrogenation and consequent dehydrogenation curves of 1000 complete cycles for the nanocomposite powders obtained after 50 h of milling time are presented in (e). HRTEM images of the nanocomposite powders subjected to 300 and 1000 cycles are presented in (f) and (g), respectively.[88]

100 s and 613 s, respectively.[93] At this temperature, the synthesized nanocomposite powders possessed an excellent absorption/desorption cyclability of 2546 complete cycles within 1250 h.[11] However, a minor degradation (~0.5 wt% H_2) in the hydrogen storage capacity was observed after 2546 h of the cycle-life-time, owing to a minor grain growth that came off in the metallic Mg and Zr_2Ni grains. It is worth mentioning that Zr_2Ni maintained its big-cube structure (fcc) after the long cyclic processing time, suggesting it has a good stability against an applied cyclic pressure and temperature.

The first report of using metallic glassy (MG) $Zr_{70}Ni_{20}Pd_{10}$ nanopowders as a catalytic agent to enhance the hydrogenation/dehydrogenation kinetics of MgH_2 was introduced by El-Eskandarany in 2016.[24] In his work, nanocrystalline MgH_2 powders prepared using the RBM technique were doped with small mole fractions (5 wt%) of MG-$Zr_{70}Ni_{20}Pd_{10}$ powders and then high energy ball-milled for 50 h under 50 bar of H_2. The HRTEM image taken near the edge of the MgH_2/5 wt% amorphous $Zr_{70}Ni_{30}Pd_{10}$ composite particle obtained after 50 h of RBM time is shown in Fig. 15a together with the corresponding nano-beam diffraction pattern (NBDP) (Fig. 15b). Overall, the composite powders obtained after this stage of milling consisted of a continuous amorphous matrix (maze-like morphology; Fig. 15a) hosting ultrafine nanoclusters (~4 nm in diameter) of an ordered-structure (related to MgH_2).

It is worth mentioning that the MgH_2 grains were distributed into the metal glassy powders in a segregated fashion with the absence of agglomerates or aggregated grains, as displayed in Fig. 15a. The NBDP shows that a halo-diffraction pattern related to amorphous $Zr_{70}Ni_{30}Pd_{10}$ coexisted with a spot-like pattern which originated from the nanocrystalline γ- and β-MgH_2 phases oriented in different axial directions.[94] The end-product (50 h) of the MgH_2/5 wt% MG-$Zr_{70}Ni_{20}Pd_{10}$ nanocomposite powders consisted of fine powders in the range between 180 to 500 nm, as presented in Fig. 16a. The scanning transmission electron microscopy-bright field imaging (STEM-BFI) and the corresponding scanning transmission electron microscopy-dark field imaging (STEM-DFI) of a selected nanocomposite MgH_2/5 wt% MG-$Zr_{70}Ni_{30}Pd_{10}$ powder particle are shown in Fig. 16a and b, respectively. The powders had an almost spherical-like morphology (Fig. 16b), containing fine lenses of less than 10 nm in diameter that were homogeneously distributed into the metallic glassy matrix (Fig. 16c and d). The fine spherical lenses corresponded to Mg (Fig. 16c), and the elemental mappings of Zr, Ni and Pd are presented in Fig. 16d, e, and f, respectively. The EDS-analysis indicated an excellent elemental distribution beyond the sub-micro level.[24]

Fig. 17a and b shows the PCT curves determined at 200 and 350 °C for the nanocomposite MgH_2/5 wt% MG-$Zr_{70}Ni_{30}Pd_{10}$ powders obtained after 50 h of ball milling (Fig. 17a) and the MgH_2 powders obtained after 6 h of RBM time (Fig. 17b), respectively. For successful hydride formation (complete absorption) of the pure MgH_2 sample, a high temperature (350

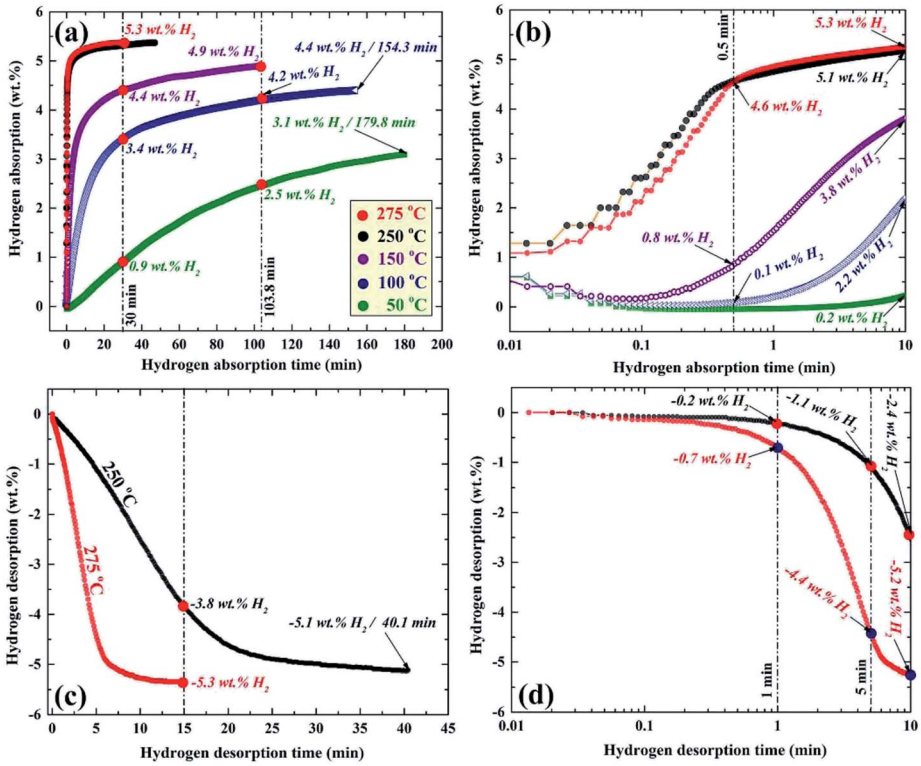

Fig. 14 Temperature and time effects on the (a and b) hydrogenation, and (c and d) dehydrogenation kinetics of nanocomposite MgH_2/10 wt% $ZrNi_5$ powders obtained after RBM for 50 h.[89]

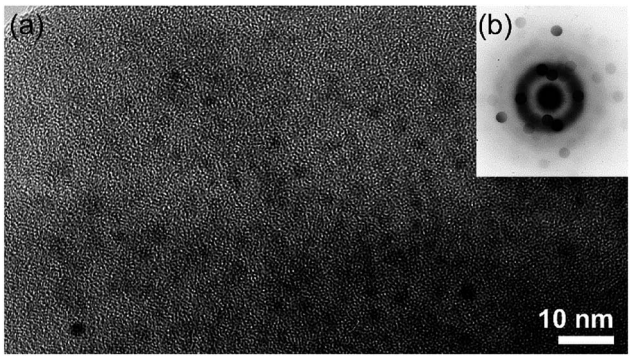

Fig. 15 (a) HRTEM image of MgH_2 powders doped with 5 wt% $Zr_{70}Ni_{30}Pd_{10}$ and milled for 50 h, and (b) the corresponding NBDP.[90]

°C) and pressure (P_{abs}, in the range between 200 mbar to 40 bar) were required to absorb approximately 4.7 wt% H_2, as shown in Fig. 17b. This indicates that the sample requires the application of a higher temperature to achieve the theoretical hydrogen storage capacity (7.6 wt% H_2).

Pure MgH_2 showed a poor dehydrogenation behavior, this is exhibited by the clear pressure hysteresis with significant large gaps (~17 bar) between the pressure needed for absorption (hydride formation), P_{abs} and the pressure required for hydride decomposition, P_{des}, as presented in Fig. 17b. In addition, pure MgH_2 powders obtained after 6 h of RBM time failed to release the stored hydrogen content completely, even after 12 h of desorption time (Fig. 17b). In contrast to the pure MgH_2 sample, the nanocomposite powders showed excellent PCT hydrogenation/dehydrogenation curves, demonstrated by the complete hydrogen sorption/desorption event at a lower temperature (200 °C) and pressure (50 mbar to 10 bar), as shown in Fig. 16a.

At a relative low temperature and pressure, the nanocomposite sample reached a higher value of hydrogen storage capacity (5.8 wt%) when compared with pure MgH_2 (4.7 wt% H_2). Moreover, the plateau region for the nanocomposite sample was very flat with a negligible slope and with the absence of multistep hydrogenation/dehydrogenation, as shown in Fig. 17a. In addition, the sample succeed to achieve complete desorption through an almost flat PCT curve with a minimal difference value (~72 mbar) between the P_{abs} and P_{des}, as shown in Fig. 17a. Complete hydrogenation (Fig. 17c)/dehydrogenation (Fig. 17d) processes were successfully achieved with fast kinetics to charge/discharge about 6 wt% H_2 at 200 °C within 1.18 min/3.8 min, respectively.[24] In addition, this new nanocomposite system shows a high performance, achieving 100 continuous hydrogen charging/discharging cycles without degradation, as elucidated in Fig. 17e.

5.2 Mechanism of enhancing MgH_2 kinetics upon doping with abrasive powders

The present review article, which focuses on using selected abrasive powders of metal oxides, metal carbides, metal hydrides, and metastable Zr-based alloys, has shown that these catalytic agents are heterogeneous, in that they do not react with MgH_2 to form an intermediate reactive phase with improved

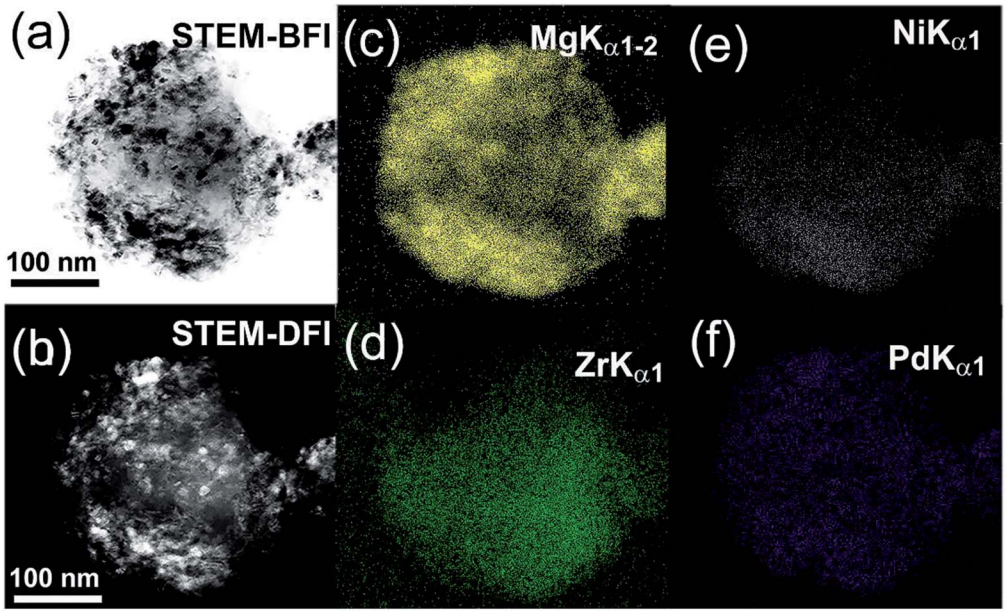

Fig. 16 STEM-BFI and STEM-DFI images for MgH_2 powders doped with 5 wt% $Zr_{70}Ni_{30}Pd_{10}$ are displayed in (a) and (b), respectively. The X-ray-elemental mapping for Mg, Zr, Ni and Pd corresponding to (a) are presented in (c–f), respectively.[24]

storage properties. Using the metallic glassy $Zr_{70}Ni_{20}Pd_{10}$ powders, which did not undergo any structural changes or react with MgH_2 up to 200 °C,[24] as a typical example, we found that during the early stage of ball milling the ball-powder-ball collisions of MgH_2 doped with abrasive nanopowders (micro-milling media) (Fig. 18a), led to break down of the large MgH_2 powder particles and assisted the adherence of the fine powders onto the surface of the MgH_2 particles (Fig. 18b). At this stage of

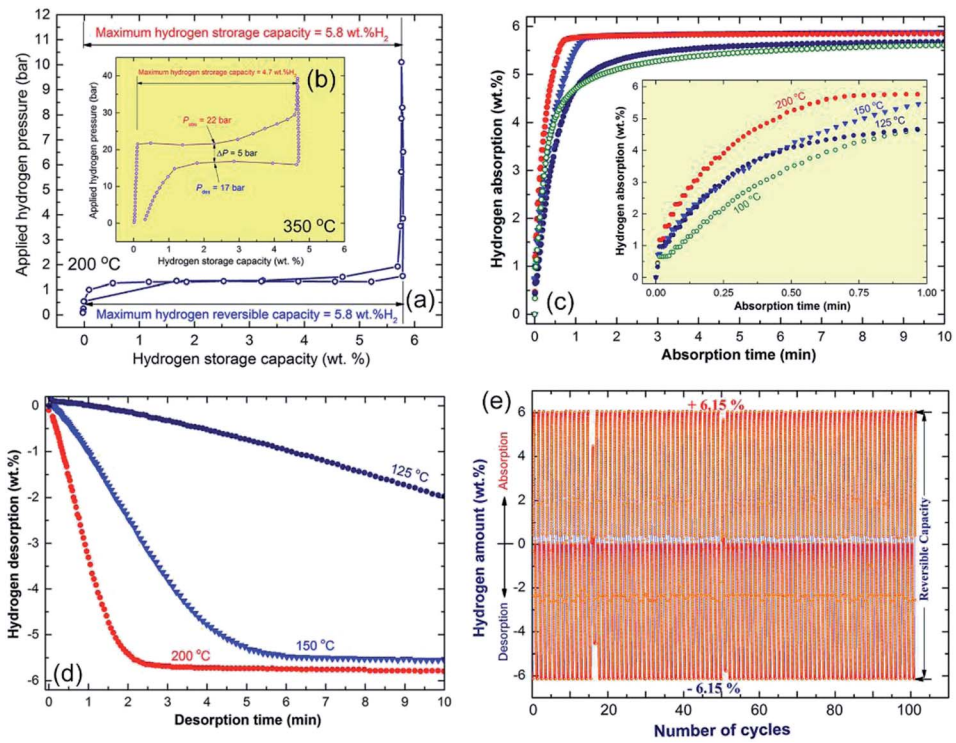

Fig. 17 The PCT curves for the end-products of the ball-milled MgH_2/5 wt% metallic glass $Zr_{70}Ni_{20}Pd_{10}$ nanocomposite and MgH_2 powders are shown in (a and b), respectively. Insets: the PCT experiment conducted at 200 °C for the nanocomposite powders (a), was accomplished at 350 °C for the MgH_2 system (b). The hydrogenation/dehydrogenation kinetics for the MgH_2/5 wt% metallic glass $Zr_{70}Ni_{20}Pd_{10}$ nanocomposite and MgH_2 powders as a function of the applied temperature are presented in (c) and (d), respectively. The cycle-life-time test for the end-product of the nanocomposite powders conducted at 200 °C is displayed in (e).[24]

milling, the hard nanopowders penetrated the oxide layer formed on the surfaces of the MgH_2 powders to create micro-holes on their surfaces (Fig. 18c).

Increasing the ball milling time led to "migration" of a large volume fraction of the abrasive milling media powders through the cavities and micro-channels created in the body of the MgH_2 particles and located at their grains. Hence, they break up the large MgH_2 grains along with their weak grain boundary zones (Fig. 18d) and form finer powders with a large volume fraction of nanostructured grains (Fig. 18e). As hydrogen diffusion is much faster along the grain boundaries when compared with inside the grains, the hydrogenation/dehydrogenation kinetic behaviors of MgH_2 were gradually improved by increasing the number of "liberated" grains. During the last stage of ball milling, the role of the ball-powder-ball collisions in achieving further refining of the MgH_2 powder particles was almost absent as the size of the powders became ultrafine (less than 1 μm). Accordingly, the final refining process was attained by the nanosized abrasive milling media, which were homogeneously distributed within MgH_2 to form typical homogeneous nanocomposite powders (Fig. 18f).

5.3 Development of high performance pure MgH_2 by severe plastic deformation

In spite of the beneficial effects obtained upon doping MgH_2 with catalytic agents, these additives always lead to a significant decrease in the hydrogen storage capacity.[91] Apart from doping MgH_2 powders with catalysts, it has been experimentally demonstrated by some authors that changing the crystal structure of the stable β-tetragonal MgH_2 phase to a less stable phase of γ-orthorhombic MgH_2 leads to improved gas uptake/release kinetics and a decrease in the hydrogenation temperature without a drastic decrease in the storage capacity.[91–93] β-to-γ phase transformations can be attained *via* severe plastic deformation (SPD)[94] at ambient temperature using different approaches such as HEBM,[95] cold rolling,[96] equal channel angular pressing (ECAP),[97] and high pressure torsion (HPT).[98] Commonly the results of these employed techniques demonstrated that formation of a nanocrystalline phase along with introducing high intensity defects, leads to an increase of the density of the grain boundaries. The presence of these defects in the Mg lattice leads to the creation of nucleation points for hydrogenation, in which the existence of a large number of grain boundaries assists fast diffusion pathways for hydrogen.[99]

Recently, a new metastable MgH_2 nanocrystalline powder was discovered by a group at KISR.[100] In that study, the as-prepared MgH_2 powders were charged and sealed in a stainless steel (SUS304) tube (0.8 cm diameter and 20 cm length) inside a glove box under a helium gas atmosphere, as shown in Fig. 19a. The tube contained MgH_2 powders that had undergone a severe CR process for a different number of passes (1 to 200 passes), using two-drum type manual cold rollers (11 cm wide × 5.5 cm in diameter), as displayed in Fig. 19b.

After 25 passes, the powders were agglomerated and formed large aggregates upon CR for 25 passes (Fig. 19c and d). After 200 passes, micro-bands with a thickness of 143 mm were developed

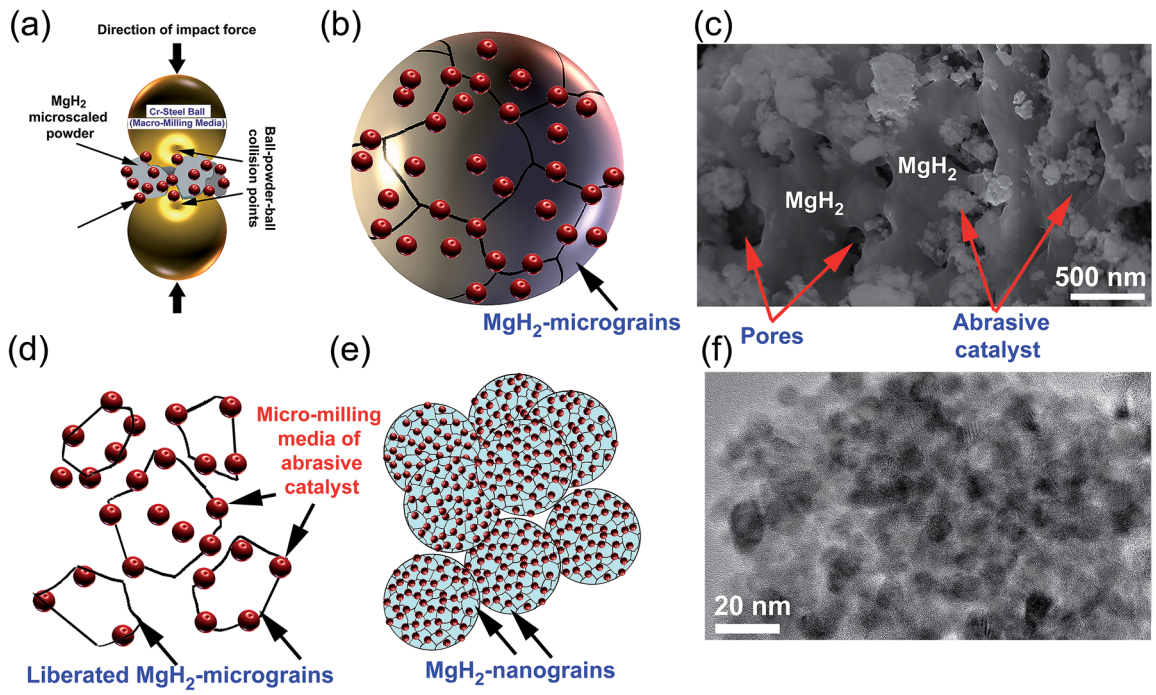

Fig. 18 A schematic illustration showing a mixture of MgH_2 and metallic glassy $Zr_{70}Ni_{20}Pd_{10}$ powders that were charged in a stainless steel vial together with stainless steel balls. The large MgH_2 powders were subjected to severe mechanical deformation upon high-speed ball-powder-ball collisions (a), leading to disintegration into smaller particles. The red-colored spheres shown in (b) represent the ultrafine metallic glassy powders adhered on the surface of the metal hydride powders. These hard spherical metallic glassy powders penetrate the surface of the MgH_2 powders and create pores (c). The metallic glassy powders play an important role as abrasive micro-milling media and the led to liberation of the MgH_2 grains (d). Continuous disintegration takes place with a further increase in the milling time (e), in which the end product possesses an ultrafine morphological structure (f).

as a result of cold working generated during the CR process (Fig. 19e). The as-prepared powders that underwent 200 CR passes were then subjected to HEBM under hydrogen gas for 50 h.

The XRD pattern of the CRed MgH_2 powders obtained after 200 CR passes and then after HEBM for 50 h are displayed in Fig. 20a. Obviously, the Bragg peaks corresponding to the γ- and β-MgH_2 phases completely vanished and were replaced with new Bragg peaks for a unreported phase, which appeared at scattering angles (2θ) of 35.034, 40.584, 58.758, 70.115, and 73.868 (Fig. 20a).

X-ray diffraction analysis (XRD) analysis indicated that this newly discovered MgH_2 phase has a face centered cubic structure (fcc) of space group, $Fm\bar{3}m(225)$. The lattice parameter (a_o) for this phase, calculated from (111) was 0.44361 nm.[100] The FE-HRTEM image of the powders cold rolled for 200 passes and then treated with HEBM for 50 h is shown in Fig. 20b. The image revealed a Moiré fringe image for the three related nanograins. Filtered-fringe images corresponding to Zone I are presented in Fig. 20b. The d-spacing related to fcc-MgH_2 (111) was calculated and found to be 0.2559 nm, in which the corresponding a_o was calculated and found to be 0.4433 nm. These values matched well with the results from the XRD analysis. The FFT image, which is displayed in Fig. 20c, was taken from Zone I and oriented to the [001] axis, and the corresponding FFT showed a spot-electron diffraction pattern related to fcc-MgH_2 (111), as presented in Fig. 20d.

Fig. 21 displays the dehydrogenation kinetic behaviors of the cold rolled powder obtained after 200 passes and then after HEBM for 50 h (fcc-MgH_2 phase). The measurements were conducted in the temperature range of 175 to 275 °C under 200 mbar without powders activation, and after activating the powders at 300 °C under 10 bar H_2 (Fig. 21b). In order to maintain the crystal structure of the powders (fcc-MgH_2 phase) obtained after this stage of milling, the desorption kinetic

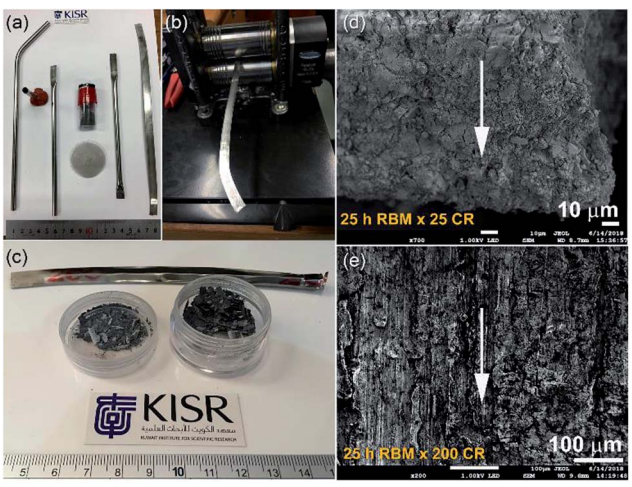

Fig. 19 (a) The reactive ball milled MgH_2 powders obtained after 25 h of HEBM under hydrogen were charged into SUS304 tubes and then cold-rolled for 200 passes (b). (c) A photograph of the powders obtained after 25 passes. FE-SEM micrographs taken at an accelerated voltage of 1 kV of MgH_2 powders obtained after 25 h of RBM and then after CR for (d) 25, and (e) 200 passes.[100]

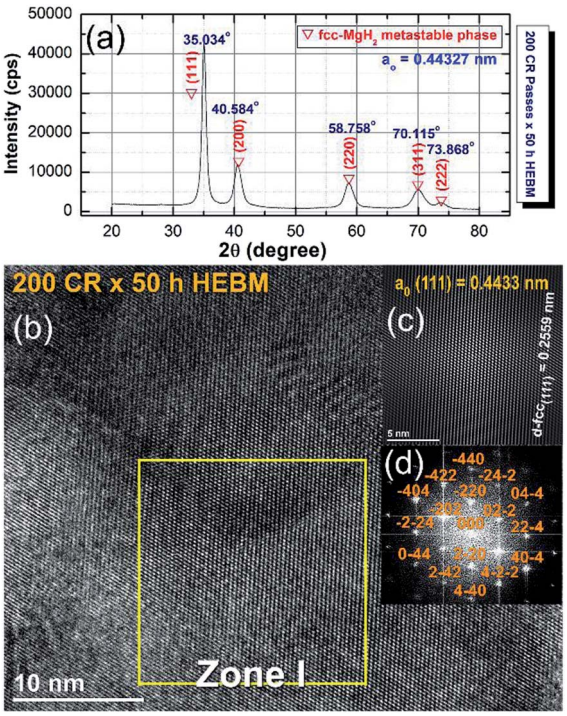

Fig. 20 (a) XRD pattern of cold rolled MgH_2 powders obtained after 200 passes and then HEBM for 50 h. (b) FE-HRTEM image; (c) filtered atomic resolution image of Zone I, and (d) FFT image of the MgH_2 powders obtained after 25 h of RBM, then subsequently cold rolled for 200 passes and finally after HEBM for 50 h.[100]

measurements were taken without activation for five individual samples (Fig. 21a). All of the samples successfully desorbed their hydrogen storage with different time scales. Generally, the fcc-MgH_2 powders showed advanced dehydrogenation characteristics compared to the γ- and β-MgH_2 phases.

At 175 °C, the sample desorbed ~4 wt% H_2 within 40 min (Fig. 21a). However, the powders desorbed about 6.5 wt% H_2 within 22 min at 200 °C (Fig. 21a). Increasing the applied temperature to 225 and 250 °C, improved the dehydrogenation kinetics of fcc-MgH_2, indicated by the short time required to desorb 6.6 wt% H_2 in 17 min and 10 min, respectively (Fig. 21a). Outstanding desorption kinetics were found at 275 °C, when the sample desorbed 6.6 wt% H_2 within 7 min, as elucidated in Fig. 21a. We should emphasize that the XRD patterns for the examined samples at a temperature range between 175 to 225 °C revealed the presence of Bragg peaks corresponding to the γ- and β-MgH_2 phases. However, the XRD patterns for the samples examined at higher temperatures (250 and 275 °C) revealed diffraction lines for the hcp-Mg phase.

Fig. 21b displays the dehydrogenation kinetics conducted for the same samples shown in Fig. 21a, however, they were activated first at 300 °C (far above the transformation temperature of the fcc-MgH_2 to γ- and β-MgH_2 phases[101]) and under 25 bar H_2. Based on this activation step condition, all of the samples lost their fcc-structure and completely transformed into γ- and β-MgH_2 phases. This led to a significant reduction in the dehydrogenation kinetics, which became slow when compared

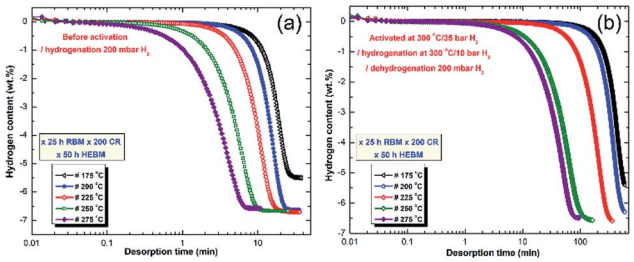

Fig. 21 Dehydrogenation kinetics measured for 10 individual samples of MgH_2 powders obtained after 25 h of RBM, and subsequently cold rolled for 200 passes and then HEBM for 50 h. The measurements were conducted under 200 mbar H_2 (a) without powder activation, and (b) after activating the powders at 300 °C under 10 bar H_2.[100]

with the same samples shown in Fig. 21a. For example, the sample examined at 175 °C required more than 650 min to desorb less than 5.5 wt% H_2 (Fig. 21b). The two samples examined at 200 and 225 °C desorbed about 6.4 and 6.6 wt% H_2 within 600 and 390 min, respectively (Fig. 21b). By comparing the necessary desorption time (100 min) for the sample examined at 275 °C to release 6.6 wt% H_2 (Fig. 21b) with the time required (7 min) for the fcc-MgH_2 sample (Fig. 10a) to desorb same hydrogen amount at the same temperature, we can see that the kinetics desorption of the fcc-MgH_2 phase is 14 time faster than the γ- and β-MgH_2 phases.

6. MgH_2 for FC applications

In 2007, de Rangeo *et al.*[102] reported the possibility of employing nanostructured MgH_2 as a hydrogen storage media for a pilot reactor tank. In their study, a small-scale tank was developed and tested in different cooling conditions. At 280 °C, the system absorbed 4.9 wt% H_2. The authors reported that it is essential to maintain the material below 370 °C to avoid the rapid crystal growth of Mg powders associated with a strong degradation of the kinetics of the hydriding/dehydriding reactions.[102]

Same authors succeeded in enhancing the hydrogen sorption of MgH_2, they used it in their first reactor model by mixing it with expanded natural graphite (ENG) and consolidating the powders into compacted disks.[103] They reported that incorporating ENG before compression drastically improves the thermal conductivity in the direction normal to the compression axis. Moreover, the thermal conductivity increases linearly with the ENG content, and can be adjusted to fulfill the loading time requirements.[103] Since then, different schools have introduced various studies focused on the design and manufacture of hydrogen reactors based on the MgH_2-system.[104–106]

Based on the 8th Strategic Plan of KISR (2015–2020) for NAM/EBRC which concerns employing as-prepared Mg-nanocomposite powders for PEM-FC applications, we succeeded in implementing MgH_2/10 wt% (8 Nb_2O_5/2 Ni) nanocomposite buttons in the charging of a cell-phone battery, using a homemade integrated Ti-tank/PEM-FFC system. Fig. 22 displays a summary of the experimental procedure for charging the Ti-reactor using the buttons, and Fig. 23 presents the setup of the Ti-tank/PEM-FFC integrated system. More details are presented elsewhere.[17]

The hydrogen released from the nanocomposite buttons upon heating of the storage system to 225 °C was used to feed the PEM-FC. Fig. 24a presents the experimental set up utilized for charging the battery of a cell phone device through a 5 V voltage regulator. The PEM-FC system is controlled and operated using software in which the data output corresponding to the hydrogen flow rate, voltage and current were obtained and stored. During the first few min (0.033 min) of the battery charging time, conducted at 225 °C the MgH_2 powders were completely decomposed, and the pressure of the released hydrogen was saturated at a value of 20 bar, as indicated in Fig. 24c. To avoid any reaction between the Mg powders and the hydrogen gas released and stored inside the Ti-tank, the heating

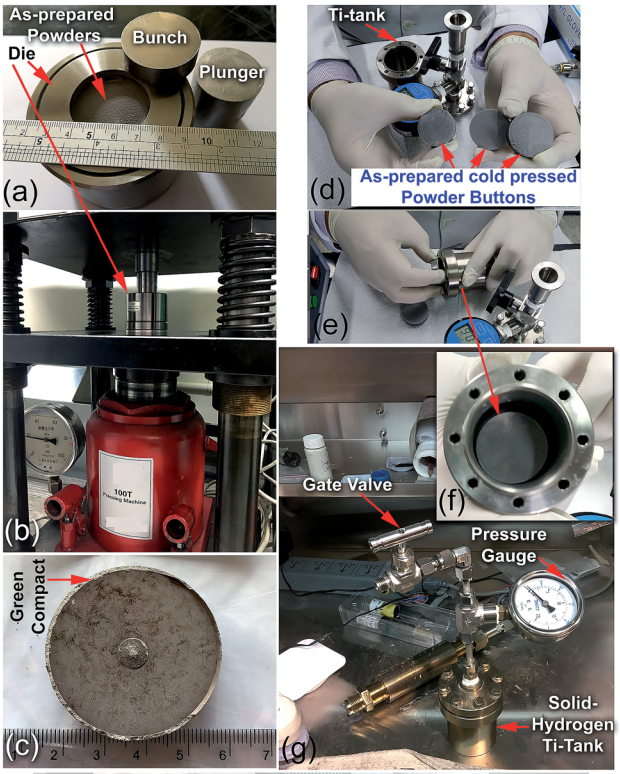

Fig. 22 Preparation procedure used for the fabrication of the nanocomposite MgH_2/8 wt% Nb_2O_5/2 wt% Ni disks. (a) About 30 g of the as-prepared nanocomposite powders were charged into a 3.25 mm-diameter tool steel powder die and sealed with upper/bottom bunches, and the plunger in the glove box was filled with a He gas atmosphere. The system was then subjected to an axial vertical load of 20 tons at ambient temperature for 50 h, using a 100 ton cold press (b). The as-prepared cold pressed solid-hydrogen nanocomposite system had a relative density of ~68.7% (c). Three cold-pressed nanocomposite bulk samples with a total weight of about 87 g were placed into a high-pressure hollow vessel made of pure titanium metal (hydrogen tank) with the following dimensions: 8 cm high × 6.2 cm outer diameter × 5.4 cm inner diameter (d–f). The system was sealed with eight hexagonal bolts (hexagonal head cap screws) and connected to a high-pressure gate ball-valve with a 20 bar pressure gauge inside the glove box filled with He gas (g).[17]

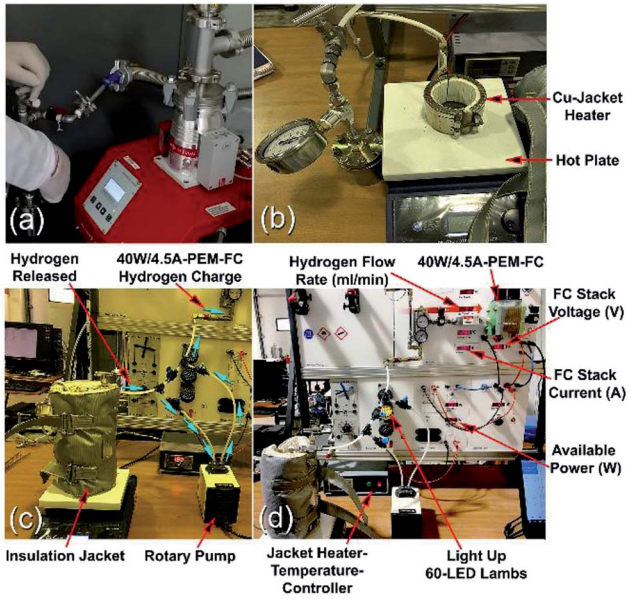

Fig. 23 Solid-hydrogen storage tank integrated with a 40 W/4.5 A PEM-FC system. (a) The Ti-tank containing the nanocomposite disks was evacuated using a rotary/molecular pump; (b) the temperature controlled hotplate and Cu-jacket heater; (c) the Ti-tank hydrogen storage system was filled with MgH_2/8 wt% Nb_2O_5/2 wt% Ni nanocomposite disks; and (d) the solid-hydrogen tank was coupled with a 40 W/4.5 A PEM-FC.[17]

process for the system was immediately stopped. Then, the ball gate valve was opened and the rotary pump facilitated the succession of H_2 towards the PEM-fuel cell (Fig. 25).

The monotonical decrease of the H_2 pressure inside the Ti-tank upon increasing the battery charging time implies that a continuous amount of hydrogen gas was delivered to the PEM-fuel cell. It should be mentioned that using a rotary pump led to delivery of the hydrogen gas to the fuel cell at a constant rate of ~160 ml min^{-1}, as shown in Fig. 24b.

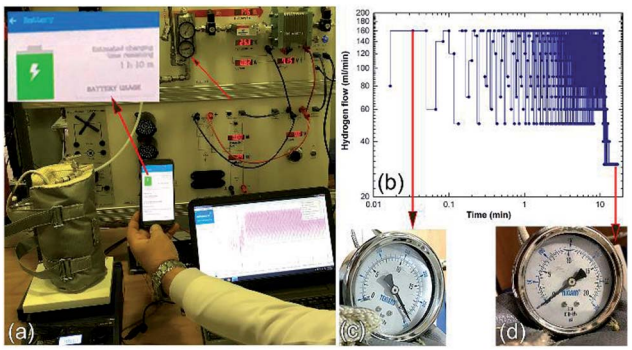

Fig. 24 Charging of a battery for a cell phone device *via* a solid-hydrogen storage tank integrated with a 40 W/4.5 A PEM-FC system. (a) The hydrogen storage system filled with MgH_2/8 wt% Nb_2O_5/2 wt% Ni nanocomposite disks coupled with 40 W/4.5 A PEM-FC to charge the battery of a cell phone device. The hydrogen flow during the cell-phone charging process is displayed in (b) as a function of the battery charging time, (c) and (d) show the hydrogen pressure of the Ti-tank at the initial and final charging stages, respectively.[17]

7. Conclusions and closing remarks

Developing alternate energy sources has become necessary for the sustainable common future of our planet. Nowadays, invention and innovations dedicated to discovering advanced green energy systems are rapidly moving towards real applications. Accordingly, research activities related to alternative energy have recently been considered as excellent opportunities for starting promising new businesses.

For a long time, hydrogen has been seriously considered to be an ideal energy carrier and it has a tremendous amount of attractive properties, making it a unique clean energy option for the future. Despite this, hydrogen does not show fast growth owing to critical issues linked to the high cost required for production and intellectual technical challenges related to the transportation and storage. Hydrogen storage, which spans both hydrogen production and hydrogen applications, plays an important role in initiating a hydrogen economy.[107]

Within the last three decades, this subject has received significant attention, demonstrated by the great number of intensive research activities related to this important area.[107] Apart from the traditional methods of hydrogen storage, hydrogen can be successfully stored with a high gravimetric density in some light metals such as Li, Be, Na, Mg and Al. In spite of the high mass density of LiH (12.6 wt%) and BeH_2 (18.2 wt%), they decompose at a very high temperature which restricts their fuel cell applications. Moreover, NaH, which releases hydrogen in a temperature range between 430 and 500 °C, has a very low storage capacity of 4.2 wt%. Although AlH_3 has a good storage capacity (10 wt%) and a relatively low decomposition temperature (60–140 °C), AlH_3 is not reversible. Schneemann *et al.*[108] have recently published an important review article, discussing the potential applications of different nanostructured metal hydrides and their hydrogen storage properties.[108]

MgH_2, with its high storage capacity (7.6 wt%), great cyclability, natural abundance, and low cost has been considered as the most suitable hydrogen storage material for fuel cell applications. Unfortunately, MgH_2 has several drawbacks related to its high thermal stability, slow kinetics of hydrogenation and dehydrogenation and high apparent activation energy. All of these disadvantages restrict its immediate employment in fuel cell applications. Within the last few years,

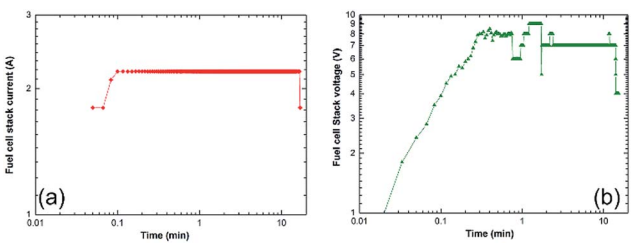

Fig. 25 Correlation between the charging time and (a) the fuel cell-stack current, and (b) the voltage upon the charging of a cell phone battery *via* a solid-hydrogen storage tank integrated with 40 W/4.5 A PEM-FC system.[17]

many review articles have presented and discussed the possibility of designing Mg-based nanomaterials for hydrogen storage.[107–109] In 2017, a comprehensive review article published by Zhang *et al.* presented the recent progress achieved to improve MgH_2 through catalytic agents and nanoconfinement.[110]

Mg and Mg_2Ni were suggested 52 years ago as being suitable for use in internal combustion engines in the car industry.[110] In this work, the heat generated from the exhaust gas of the vehicle was utilized as the heat necessary for releasing hydrogen.[111,112] In addition, Mg-based materials, in particularly Mg_2Ni alloy, have been extensively proposed for waste heat recovery and for use as thermal batteries for concentrating solar thermal power.[109,113] Recently, Sheppard *et al.* published a very important review article discussing the potential applications of using metal hydrides, in particularly Mg-based alloys, concentrating on thermal power storage applications.[114]

This review article has presented the enormous efforts devoted to improving the hydrogenation and dehydrogenation behaviors of MgH_2 through three strategies. The philosophy of the first strategy depends on melting metal Mg with alloying element(s) to reduce the high enthalpy change of formation for MgH_2 and to enhance the kinetics. Using heavy metals such as Ni, Pd, and Nd leads to a significant reduction in the storage capacity of MgH_2 with no significant improvement in the decomposition temperature.

In the second strategy, MgH_2 is mechanically-doped with different types of catalyst/nanocatalysts, using HEBM under reactive hydrogen or inert gas. The catalysts used in this approach can be classified into pure metals, intermetallic compounds and alloys, metal oxides, metal/metal oxide nanocomposites, and hard refractory materials of metal carbides and nitrides. In contrast to the first strategy, doping MgH_2 with some typical nanocatalysts such as Nb_2O_5, V_2O_5, Cr_2O_3, composites of Ni/Nb_2O_5, TiC, $Ti_{0.4}Cr_{0.15}Mn_{0.15}V_{0.3}$, TiH_2, and NbH have shown outstanding beneficial effects in improving the gas uptake/release kinetics and reduction of both the hydrogenation/dehydrogenation temperature and apparent activation energy of decomposition. However, doping the hydride phase with a high volume fraction of catalytic agents (above 10 wt%) always leads to a significant degradation in the storage capacity.

The philosophy of the last strategy depends on introducing a heavy network of lattice imperfections and defects to Mg, pure MgH_2, and Mg-based alloys without using any type of catalyst. This mechanical treatment regime has been successfully achieved by subjecting the powders to long-term HEBM through mechanically-induced cyclic phase transformations. β–γ and cyclic β–γ–β phase transformations are always coupled with a dramatic decrease in the grain sizes of the MgH_2 powders. As hydrogen diffusion along the grain boundaries is much faster than diffusion in the side grains, the hydrogenation/dehydrogenation kinetics of MgH_2 are dramatically improved upon production of such fine nanostructured grains, containing a large number of grain boundaries.

Furthermore, this work elucidated the research activities related to hydrogen storage taking place at the Kuwait Institute for Scientific Research since 2010. Like many other international laboratories in the world, we aim to develop and implement new categories of MgH_2-based nanocomposites for fuel cell applications. Our strategy is dedicated to synthesizing and improving MgH_2-materials based on employing RBM techniques under a hydrogen atmosphere to synthesize nanocrystalline MgH_2 powders. Our results have shown that cold rolling of as-prepared milled MgH_2 powders led to a superior improvement in the kinetics without drastic decreasing the storage capacity. In addition, we have employed a micro-milling media of abrasive metal oxides, metal carbides, and intermetallic compounds, as well as metastable powders for refining MgH_2 grains. The nanocomposite MgH_2/abrasive micro-milling powders possessed excellent hydrogenation/dehydrogenation kinetics with very long charging/discharging cyclability at rather low temperatures. We also introduced a new *in situ* catalytic approach for doping MgH_2 powders through a single step, using a solid ball-milling media.

Conflicts of interest

There are no conflicts to declare.

Acknowledgements

The author would like to express his sincere gratitude to Dr Samira A. S. Omar, the Director General of the Kuwait Institute for Scientific Research for her continuous encouragement and support. I would like also to express my very great appreciation to Dr Osamah Alsayegh, the Executive Director of the Energy and Building Research Center, Kuwait Institute for Scientific Research for his great and continuous support. I am particularly grateful for the technical support given by my colleagues, working in the Solid-State Hydrogen Storage Materials group, the Nanotechnology and Advanced Materials Program, Energy and the Building Research Center, at the Kuwait Institute for Scientific Research. The financial support received by the Kuwait Government through the Kuwait Institute for Scientific Research for purchasing the equipment used in the present work using the budget dedicated to the project led by the author (P-KISR-06-04) at the Establishing Nanotechnology Center in KISR, is highly appreciated. Appreciation is extended to the Kuwait Foundation for the Advancement of Sciences (KFAS) for the partial financial support of this study related to Project EA061C under contract number: P315-35EC-01 and Project EA078C under contract number: PR1814SP12. The financial support received from Kuwait Petroleum Corporation (KPC) for purchasing the golf cart used in the present investigation is highly appreciated.

Notes and references

1 International Energy Agency, *Key world energy statistics*, 2017, https://www.iea.org/publications/freepublications/publication/KeyWorld2017.pdf.
2 Energy Information Administration (EIA), *U.S. energy-related carbon dioxide emissions, 2014*, U.S. Department of

Energy, Washington, DC, 2015, Online at http://www.eia.gov/environment/emissions/carbon/, accessed on January 12, 2019.
3 R. B. Jackson, C. Le Quéré, R. M. Andrew, J. G. Canadell, G. P. Peters, J. Roy, *et al.*, *Environ. Res. Lett.*, 2017, **12**, 110202, DOI: 10.1088/1748-9326/aa9662.
4 W. I. F. David, *Faraday Discuss.*, 2011, **151**, 399–414.
5 P. T. Latake, P. Pawar and A. C. Ranveer, *International Journal of Innovative Research and Creative Technology*, 2015, **1**, 333–337.
6 S. Maryam, *Int. J. Hydrogen Energy*, 2017, **42**, 24927–24938.
7 G. Marbán and T. Valdés-Solís, *Int. J. Hydrogen Energy*, 2007, **32**, 1625–1637.
8 E. Lanzia, E. Verdolinia and I. Haščič, *Energy Policy*, 2011, **39**, 7000–7014.
9 S. Banerjee and A. K. Tyagi, *Functional Materials Preparation, Processing and Applications*, Elsevier, 1st edn, 2011, ISBN: 9780123851420.
10 M. Moreno-Benito, P. Agnolucci and L. G. Papageorgiou, *Comput. Chem. Eng.*, 2017, **102**, 110–127.
11 M. Sherif El-Eskandarany, H. Al-Matrouk, E. Shaban and A. Al-Duweesh, *Energy*, 2015, **91**, 274–282.
12 G. Walker, *Solid-state hydrogen storage: Materials and Chemistry*, Woodhead Publishing Limited, New York, 1st edn, 2008, ch. 1.
13 T. N. Veziroğlu and S. Sümer, *Energy Convers. Manage.*, 2008, **49**, 1820–1831.
14 M. S. El-Eskandarany, *Mechanical Alloying: Nanotechnology, Materials Science and Powder Metallurgy*, Elsevier Inc., Oxford, 2nd edn, 2015, ch. 9.
15 L. Schlapbach and A. Züttel, *Nature*, 2001, **414**, 353–358.
16 M. Sherif El-Eskandarany, E. Shaban, F. Aldakheel, A. Alkandary, M. Behbehani and M. Al-Saidi, *Sci. Rep.*, 2018, **7**, 13296, DOI: 10.1038/s41598-017-13483-0, http://www.nature.com/scientificreports, .
17 M. Sherif El-Eskandarany, E. Al-Nasrallah, M. Banyan and F. Al-Ajmi, *Int. J. Hydrogen Energy*, 2018, **27**, 23382–23396.
18 T. Sinigaglia, F. Lewiski, M. E. S. Martins and J. C. M. Siluk, *Int. J. Hydrogen Energy*, 2017, **42**, 24597–24611.
19 G. Walker, *Solid-state hydrogen storage: Materials and chemistry*, Woodhead Publishing Limited, New York, 1st edn, 2008, ch. 4.
20 I. P. Jain, C. Lal and A. Jain, *Int. J. Hydrogen Energy*, 2010, **35**, 5133–5144.
21 P. Moriarty and D. A. Honnery, *Int. J. Hydrogen Energy*, 2010, **35**, 12374–12380.
22 N. T. Stetson, S. McWhorter and C. C. Ahn, *Compendium of Hydrogen Energy*, ed. R. B. Gupta, A. Basile and T. N. Veziroğlu, Oxford Elsevier, 2016, ch. 1, vol. 2.
23 A. Züttel, *Mater. Today*, 2003, **6**, 24–33.
24 M. S. El-Eskandarany, *Sci. Rep.*, 2016, **6**, 26936, DOI: 10.1038/srep26936.
25 N. A. A. Rusman and M. Dahari, *Int. J. Hydrogen Energy*, 2016, **411**, 12108–12126.
26 S. Sherif, F. Barbir and T. Veziroglu, *J. Sci. Ind. Res.*, 2003, **62**, 46–63.
27 L. Z. Ouyang, H. W. Dong, C. H. Peng, L. X. Sun and M. A. Zhu, *Int. J. Hydrogen Energy*, 2007, **32**, 3929–3935.
28 R. K. Ahluwalia, T. Q. Hua and J.-K. Peng, *Int. J. Hydrogen Energy*, 2007, **32**, 3592–3602.
29 M. Ismail, *Energy*, 2015, **79**, 177–182.
30 S. A. Aceves, G. Petitpas, F. Espinosa-Loza, M. J. Matthews and E. Ledesma-Orozco, *Int. J. Hydrogen Energy*, 2013, **38**, 2480–2489.
31 A. C. Dillon, K. M. Jones, T. A. Bekkedahl, C. H. Kiang, D. S. Bethune and M. J. Heben, *Nature*, 1997, **386**, 377–379.
32 L. Angela and T. P. Yang, *J. Catal.*, 2002, **206**, 165–168.
33 M. L. Seung, H. A. Kay, Y. H. Li, S. Gotthard and F. A. Thomas, *J. Am. Chem. Soc.*, 2001, **123**, 5059–5063.
34 R. Balderas-Xicohténcatl, P. Schmieder, D. Denysenko, D. Volkmer and M. Hirscher, *Energy Technol.*, 2017, **6**, 510–512.
35 T. Graham, *Proc. R. Soc. London*, 1868, **17**, 212–220.
36 B. Sakintuna, F. Lamari-Darkrim and M. Hirscher, *Int. J. Hydrogen Energy*, 2007, **32**, 1121–1140.
37 J. M. Blackman, J. W. Patrick, A. Arenillas, W. Shi and C. E. Snape, *Carbon*, 2006, **44**, 1376–1385.
38 M. V. Lototskyy, I. Tolj, L. Pickering, C. Sita, F. Barbir and V. Yartys, *Prog. Nat. Sci.: Mater. Int.*, 2017, **27**, 3–20.
39 C. Pistidda, N. Bergemann, J. Wurr, A. Rzeszuteket, K. T. MØller, B. R. S. Hansen, *et al.*, *J. Power Sources*, 2014, **270**, 554–563.
40 R. Hardian, C. Pistidda, A.-L. Chaudhary, G. Capurso, G. Gizer, H. Cao, *et al.*, *Int. J. Hydrogen Energy*, 2018, **43**, 16738–16748.
41 M. Polanski, D. Nawra and D. Zasada, *J. Alloys Compd.*, 2019, **776**, 1029–1040.
42 J. F. Stampfer, C. E. Holley and J. F. Suttle, *J. Am. Chem. Soc.*, 1960, **82**, 3504–3508.
43 F. H. Ellinger, C. E. Holley Jr, B. B. McInteer, D. Pavone, R. M. Potter, E. Staritzky, *et al.*, *J. Am. Chem. Soc.*, 1955, **77**, 2647–2648.
44 A. Calka, *Appl. Phys. Lett.*, 1991, **59**, 1568–1570.
45 M. Sherif El-Eskandarany, K. Sumiyama, K. Aoki and K. Suzuki, *Mater. Sci. Forum*, 1992, **88**, 801–808.
46 M. Sherif El-Eskandarany, A. Alkandary, F. Aldakheel, M. Al-Saidi, F. Al-Ajmi and M. Banyan, *RSC Adv.*, 2018, **8**, 38175–38185.
47 I. P. Jain, *Int. J. Hydrogen Energy*, 2009, **34**, 7368–7378.
48 R. A. Varin, T. Czujko and Z. S. Wronski, *Nanomaterials for Solid State Hydrogen Storage*, Springer Science+Business Media, LLC, 1st edn, 2009, ch. 1.
49 C. J. Webb, *J. Phys. Chem. Solids*, 2015, **84**, 96.
50 P. Moretto, C. Zlotea, F. Dolci, A. Amieiro, J. L. Bobet, A. Borgschulte, *et al.*, *Int. J. Hydrogen Energy*, 2013, **38**, 6704–6717.
51 B. Bogdanović, K. Bohmhammel, B. Christ, A. Reiser, K. Schlichte, R. Vehlen, *et al.*, *J. Alloys Compd.*, 1999, **282**, 84–92.
52 C. P. Camirand, *Thermochim. Acta*, 2004, **417**, 1–4.
53 Y. Xiong, J. Ba, W. Qing and W. Jing, *Journal of Plasma and Fusion Research SERIES*, 2013, **10**, 94–97.

54 T. Yamada, J. Yin and K. Tanaka, *Mater. Trans.*, 2001, **42**, 2415–2421.
55 G. Liang, J. Huot, S. Boily, A. Van Neste and R. Schulz, *J. Alloys Compd.*, 1999, **292**, 247–252.
56 A. Zaluska, L. Zaluski and J. O. Ström-Olsen, *J. Alloys Compd.*, 1999, **288**, 217–225.
57 Y. Sun, C. Shen, Q. Lai, W. Liu, D.-W. Wang, K. Francois and A. Zinsou, *Energy Storage Materials*, 2018, **10**, 168–198.
58 J. Chen, G. Xia, Z. Guo, Z. Huang, H. Liu and X. Yu, *J. Mater. Chem. A*, 2015, **3**, 15843–15848.
59 X. Ding, Y. Li, F. Fang, D. Sun and Q. Zhang, *J. Mater. Chem. A*, 2017, **5**, 5067–5076.
60 A. Karty, J. Grunzweig-Genossar and P. S. Rudman, *J. Appl. Phys.*, 1979, **50**, 7200–7209.
61 J. M. Boulet and N. J. Gerard, *J. Less-Common Met.*, 1981, **89**, 151–161.
62 A. Zaluska, L. Zaluski and J. O. Ström-Olsen, *J. Alloys Compd.*, 1999, **289**, 197–206.
63 K. Dutta and O. N. Srivastava, Synthesis, *J. Mater. Sci.*, 1993, **28**, 3457–3462.
64 P. Mandal, K. Dutta, K. Ramakrishna, K. Sapru and O. N. Srivastava, *J. Alloys Compd.*, 1992, **184**, 1–9.
65 P. Wang, H. F. Zhang, B. Z. Ding and Z. Q. Hu, *Acta Mater.*, 2001, **49**, 921–926.
66 Y. Fu, M. Groll, R. Mertz and R. Kulenovic, *J. Alloys Compd.*, 2008, **460**, 607–613.
67 S. Agarwal, A. Aurora, A. Jain, I. P. Jain and A. Montone, *Int. J. Hydrogen Energy*, 2009, **34**, 9157–9162.
68 X. B. Yu, Z. X. Yang, H. K. Liu, D. M. Grant and G. S. Walker, *Int. J. Hydrogen Energy*, 2010, **35**, 6338–6344.
69 Z. Dehouche, H. A. Peretti, S. Hamoudia, Y. Yooc and K. Belkacemi, *J. Alloys Compd.*, 2008, **455**, 432–439.
70 C. Zhou, Z. Z. Fang, C. Ren, J. Li and J. Lu, *J. Phys. Chem. C*, 2013, **117**, 12973–12980.
71 C. Ren, Z. Z. Fang, C. Zhou, J. Lu, Y. Ren and X. Zhang, *J. Phys. Chem. C*, 2014, **118**, 21784–21790.
72 R. Vijay, R. Sundaresan, M. P. Maiya, S. Srinivasa Murthy, Y. Fu, H. P. Klein, *et al.*, *J. Alloys Compd.*, 2004, **384**, 283–295.
73 W. Oelerich, T. Klassen and R. Bormann, *J. Alloys Compd.*, 2001, **315**, 237–242.
74 K.-F. Aguey-Zinsou, J. R. Ares Fernandez, T. Klassen and R. Bormann, *Int. J. Hydrogen Energy*, 2007, **32**, 2400–2407.
75 N. Hanada, T. Ichikawa, S. Hino and H. Fujii, *J. Alloys Compd.*, 2006, **420**, 46–49.
76 M. O. T. da Conceição, M. C. Brum, D. S. dos Santos and M. L. Dias, *J. Alloys Compd.*, 2013, **550**, 179–184.
77 P. Wang, A. M. Wang, H. F. Zhang, B. Z. Ding and Z. Q. Hu, *J. Alloys Compd.*, 2000, **313**, 218–223.
78 I.-H. Kwon, J.-L. Bobet, J.-S. Bae and M.-Y. Song, *J. Alloys Compd.*, 2005, **396**, 264–268.
79 Z. Dehouche, T. Klassen, W. Oelerich, J. Goyette, T. K. Bose and R. Schulz, *J. Alloys Compd.*, 2002, **347**, 319–323.
80 A. Bhatnagar, S. K. Pandey, A. K. Vishwakarma, S. Singh, V. Shukla, P. K Soni, M. A. Shaz and O. N. Srivastava, *J. Mater. Chem. A*, 2016, **4**, 14761–14772.
81 R. Gupta, F. Agresti, S. L. Russo, A. Maddalena, P. Palade and G. Principi, *J. Alloys Compd.*, 2008, **450**, 310–313.
82 M. Sherif El-Eskandarany, E. Shaban, N. Ali, F. Aldakheel and A. Alkandary, Method of synthesizing MgH_2/Ni nanocomposites, *US Pat.* 9,828,245 B1, Nov. 28, 2017.
83 M. Sherif El-Eskandarany, E. Shaban, N. Ali, F. Aldakheel and A. Alkandary, *Sci. Rep.*, 2016, **6**, 37335, DOI: 10.1038/srep37335.
84 M. Sherif El-Eskandarany, E. Shaban and A. Al-Shemmiri, *Int. J. Hydrogen Energy*, 2014, **39**, 21097–21106.
85 M. Sherif El-Eskandarany and E. Shaban, *Materials*, 2015, **8**, 6880–6892.
86 M. Sherif El-Eskandarany and A. Al-Hazza, *Mater. Charact.*, 2014, **97**, 92–100.
87 M. Sherif El-Eskandarany, E. Shaban and A. Alsairafi, *Energy*, 2016, **104**, 158–170.
88 M. Sherif El-Eskandarany, H. Al-Matrouk and E. Shaban, *Int. J. Hydrogen Energy*, 2015, **40**, 10139–10149.
89 M. Sherif El-Eskandarany, E. Shaban, H. Al-Matrouk, M. Behbehani, A. Alkandary, F. Aldakheel, *et al.*, *Materials Today Energy*, 2017, **3**, 60–71.
90 M. Sherif El-Eskandarany, Composition for Hydrogen Storage, *US Pat.* 9,533,884 B1, Jan. 3, 2017.
91 X. Xiao, Z. Liu, S. Saremi-Yarahmadi and D. H Gregory, *Phys. Chem. Chem. Phys.*, 2016, **18**, 10492–10498.
92 K. Edalati, K. Kitabayashi, Y. Ikeda, J. Matsuda, H. Li, I. Tanaka, E. Akiba and Z. Horita, *Scr. Mater.*, 2018, **157**, 54–57.
93 C. Shen and K.-F. Aguey-Zinsou, *J. Mater. Chem. A*, 2017, **5**, 8644–8652.
94 R. Z. Valiev, R. K. Islamgaliev and I. V. Alexandrov, *Prog. Mater. Sci.*, 2000, **45**, 103–189.
95 M. S. El-Eskandarany, E. Shaban and B. Al-Halaili, *Int. J. Hydrogen Energy*, 2014, **39**, 12727–12740.
96 S. Amira and J. Huot, *J. Alloys Compd.*, 2012, **520**, 287–294.
97 A. M. Jorge, G. F. de Lima, M. R. M. Triques, W. José Botta and T. G. Langdon, *Int. J. Hydrogen Energy*, 2014, **39**, 3810–3821.
98 P. Vajeeston, P. Ravindran, A. Kjekshus and H. Fjellvåg, *Phys. Rev. Lett.*, 2002, **89**, 175506–175509.
99 Y. Mine, T. Tsumagari and Z. Horita, *Scr. Mater.*, 2010, **63**, 552–555.
100 M. Sherif El-Eskandarany, M. Banyan and F. Al-Ajmi, *RSC Adv.*, 2018, **8**, 32003–32008.
101 P. Vajeeston, P. Ravindran, A. Kjekshus and H. Fjellvåg, *Phys. Rev. Lett.*, 2002, **89**, 175506–175509.
102 P. de Rangeo, A. Chaise, J. Charbonnier, D. Fruchart, M. Jehan, P. Marty, *et al.*, *J. Alloys Compd.*, 2007, **446–447**, 52–57.
103 A. Chaise, P. deRango, P. Marty, D. Fruchart, S. Miraglia, R. Olives, *et al.*, *Int. J. Hydrogen Energy*, 2009, **34**, 8589–8596.
104 A. Khandelwal, F. Agresti, G. Capurso, S. L. Russo, A. Maddalena, *et al.*, *Int. J. Hydrogen Energy*, 2010, **35**, 3565–3571.
105 G. Capurso, F. Agresti, R. S. Lo, A. Maddalena, G. Principi, A. Cavallari, *et al.*, *Int. J. Hydrogen Energy*, 2011, **509S**, S646–S649.

106 S. Garrier, C. Albin, P. De Rango, P. Marty, D. Fruchart, S. Miraglia, *et al.*, *Int. J. Hydrogen Energy*, 2011, **36**, 9719–9726.
107 Y. Jiaa, C. Sunc, S. Shend, J. Zoub, S. S. Maoe and X. Yaoa, *Int. J. Hydrogen Energy*, 2015, **44**, 289–303.
108 A. Schneemann, J. L. White, S. Y. Kang, S. Jeong, L. F. Wan, E. S. Cho, *et al.*, *Chem. Rev.*, 2018, **118**, 10775–10839.
109 V. A. Yarts, M. V. Lototskyy, E. Akiba, A. Albret, V. E. Antonov, J. R. Ares, *et al.*, *Int. J. Hydrogen Energy*, 2019, DOI: 10.1016/j.ijhydene.2018.12.212.
110 J. Zhang, S. Yan and H. Qu, *Int. J. Hydrogen Energy*, 2018, **43**(3), 1545–1565.
111 L. Schlapbach, Hydrogen in intermetallic compounds II: Surface and dynamic properties, applications, *Topics in Applied Physics book series TAP*, Springer, 1992, vol. 67.
112 J.-C. Crivello, R. V. Denys, M. Dornheim, M. Felderhoff, D. M. Grant, J. Huot, *et al.*, *Appl. Phys. A*, 2016, **122**, 85.
113 J. B. von Colbe, J.-R. Ares, J. Barale, M. Baricco, C. Buckley, G. Capurso, *et al.*, *Int. J. Hydrogen Energy*, 2019, **44**(15), 7780.
114 D. A. Sheppard, M. Paskevicius, T. D. Humphries, M. Felderhoff, G. Capurso, J. Bellosta von Colbe, *et al.*, *Appl. Phys. A*, 2016, **122**, 395.